



THE UNIVERSITY *of* EDINBURGH

Edinburgh Research Explorer

Magma imaged magnetotellurically beneath an active and an inactive magmatic segment in Afar, Ethiopia

Citation for published version:

Johnson, N, Whaler, K, Hautot, S, Fisseha, S, Desissa, M & Dawes, GJK 2015, 'Magma imaged magnetotellurically beneath an active and an inactive magmatic segment in Afar, Ethiopia' Geological Society of London Special Publications, vol. 420. DOI: 10.1144/SP420.11

Digital Object Identifier (DOI):

[10.1144/SP420.11](https://doi.org/10.1144/SP420.11)

Link:

[Link to publication record in Edinburgh Research Explorer](#)

Document Version:

Peer reviewed version

Published In:

Geological Society of London Special Publications

General rights

Copyright for the publications made accessible via the Edinburgh Research Explorer is retained by the author(s) and / or other copyright owners and it is a condition of accessing these publications that users recognise and abide by the legal requirements associated with these rights.

Take down policy

The University of Edinburgh has made every reasonable effort to ensure that Edinburgh Research Explorer content complies with UK legislation. If you believe that the public display of this file breaches copyright please contact openaccess@ed.ac.uk providing details, and we will remove access to the work immediately and investigate your claim.



1 **Magma imaged magnetotellurically beneath an active and an inactive magmatic**
2 **segment in Afar, Ethiopia**

3
4 N E Johnson^{1,2}, K A Whaler¹, S Hautot³, S Fisseha⁴, M Desissa^{1,5} and GJK Dawes¹

5
6 ¹School of GeoSciences, University of Edinburgh, James Hutton Road, Edinburgh,
7 EH9 3FE

8 ²now at Stag Energy, 49 York Place Edinburgh EH1 3JD

9 ³Imagir, 38 rue Jim Sévellec, Technopôle Brest-Iroise, 29200 Brest, France

10 ⁴Institute of Geophysics, Space Sciences and Astronomy, Addis Ababa University,
11 Addis Ababa, Ethiopia

12 ⁵now at Geological Survey of Ireland, Beggars Bush, Haddington Road,
13 Dublin 4, Ireland

14
15
16 **Abstract**

17
18 We present broadband magnetotelluric data collected along profiles over two
19 magmatic segments comprising part of the sub-aerial Red Sea arm of the Afar triple
20 junction, one active since late 2005, the other currently inactive. After robust
21 processing and galvanic distortion analysis, we find the data pass the two-dimensional
22 sub-surface resistivity modelling criteria. Profiles across the segments have well-
23 defined geoelectrical strike directions parallel to the local rift axes. Data from the
24 northern end of the active segment have a more ambiguous strike that is oblique to the
25 profile and rift axis, but the direction does not have a severe impact on the model
26 deduced. All three models display prominent zones of low resistivity, interpreted as
27 arising from magma and partial melt. Petrological information has been used to
28 constrain the resistivity of the parent melt, and hence to estimate melt fractions from
29 the bulk resistivities. The total amount of melt estimated beneath the profile crossing
30 the active segment, $\sim 500 \text{ km}^3$, is approximately an order of magnitude greater than
31 that beneath the profile crossing the currently inactive rift. This implies that magma
32 availability is at least one factor affecting whether a segment is active.

33
34 **1. Introduction**

35
36 As part of a multi-disciplinary collaboration, we have collected broadband
37 magnetotelluric (MT) data along three main profiles in the Afar region of Ethiopia,
38 where the final stages of continental break-up are occurring (e.g. Wright et al., 2006).
39 The tectonic setting of our study area is shown in Figure 1, and the area itself in
40 Figure 2. Afar is the site of a rift-rift-rift triple junction where the Red Sea, Gulf of
41 Aden, and Main Ethiopian rift (the northern-most part of the East African rift system)
42 arms meet. It is separated from the Main Ethiopian rift by the Tendaho-Goba'ad
43 discontinuity, accommodating the different spreading directions and rates through
44 oblique slip (e.g. Ebinger et al., 2010). Extension in Afar is taking place primarily by
45 dyke intrusion along pre-existing zones of crustal weakness, rather than by faulting,
46 much as happens at mid-ocean ridges. It is localised into $\sim 60 \text{ km}$ long Quaternary
47 magmatic segments that are similar in size, morphology, structure, and spacing to
48 slow-spreading mid-oceanic ridge segments, and which cycle through periods of
49 activity lasting typically a decade or so and then much longer periods of quiescence

50 (e.g. Hayward and Ebinger, 1996). The segments are heavily faulted over zones of
51 ~20 km width (Rowland et al., 2007).

52
53
54

55 The main focus of the integrated study is the active Dabbahu magmatic segment, part
56 of the sub-aerial Red Sea rift, on which the recent phase of rifting began in September
57 2005, when the whole ~60 km long segment was active as a dyke intruded ~2.5 km³
58 of magma over a 2 week period, with up to 10 m of horizontal opening (Wright et al.,
59 2006; Grandin et al., 2010). This occurred in a complicated spatio-temporal pattern
60 from at least three sources, two near the Dabbahu and Gab'ho volcanoes at the
61 northern end of the segment, the other near the Ado' Ale Volcanic Complex (AVC)
62 towards its centre (Ayele et al., 2009). Magma intrusion continued for at least 3
63 months after this main event, and the associated subsidence and seismicity suggested
64 a deflating magma chamber beneath Dabbahu volcano (Ebinger et al., 2008). Another
65 13 further dykes initiating near the AVC have re-intruded the central and southern
66 section of the segment with a further ~0.5 km³ of magma, gradually relieving the
67 tectonic stress in regions of the segment associated with less opening in previous
68 intrusions (Hamling et al., 2009). GPS and InSAR data show no surface displacement
69 at the AVC associated with these dykes, except for minor subsidence following the 8th
70 in the sequence (Hamling et al., 2009). This suggests either a deep source, or that the
71 magma chamber volume is maintained by degassing as intrusion occurs, or that it has
72 large stiffness (Keir et al., 2009). Analysis of basaltic lavas from axial volcanoes
73 indicates that melting occurs at 75-100 km depth; melt ascends rapidly, with brief
74 storage at 5-7.5 km (Ferguson et al., 2010, 2013). Migrating earthquake swarms
75 associated with intrusion have been used to infer magma moving from a depth of ~8
76 km (Ebinger et al., 2008, 2010; Belachew et al., 2011).

77

78 Geochemical and petrological analyses were also carried out on suites of older
79 eruptive products, collected at the Dabbahu volcano (Field et al., 2012), one of two
80 near the northern end of the segment, and the Badi volcano, about 25 km to the west
81 of the rift axis and slightly to the north of the AVC (Ferguson et al., 2013). The ≤
82 100,000 year old Dabbahu volcano has an erupted volume of >115 km³ with a wide
83 range of magma types (Field et al., 2013). Samples from the Badi area show
84 magmatism has been occurring there for > 200,000 years (Lahitte et al., 2003), but it
85 is dormant. Badi lavas have equilibrated near the top of the mantle before being
86 transported to the surface, implying long-lived sub-crustal storage (Ferguson et al.,
87 2013).

88

89 The MT method provides information on the electrical resistivity (or equivalently its
90 inverse, electrical conductivity) of the sub-surface (e.g. Simpson and Bahr, 2005).
91 There have been many MT studies of magmatic and rifting systems, both on land and
92 in the marine environment. It has been used to investigate the plumbing system of and
93 to monitor individual volcanoes, in both subduction zone and rift environments,
94 including more recently identifying temporal changes in the data possibly arising from
95 de-gassing (e.g. Aizawa et al., 2011). It is frequently employed in the exploration of
96 hydrothermal/geothermal systems, including in identifying targets for geothermal
97 power exploitation (see the review by Munoz, 2014). It has also proved invaluable in
98 imaging the structure of and understanding the processes involved in magmatic
99 systems, including the effects of mantle plumes (e.g. Wannamaker et al., 2008; Brasse

100 and Eydam, 2008; Bologna et al., 2011; Kelbert et al., 2012). Examples of rifting
101 studies include those of Hautot et al. (2000), Simpson (2000) and Häuserer and Junge
102 (2011) further south in the East African rift, Beneath mid-ocean ridges, MT has
103 contributed to understanding mantle dynamics and the processes of melt generation
104 (e.g. Baba et al., 2006; Key et al., 2013). Our study, of a slow spreading (Fig. 1) sub-
105 ariel rifting area, has its closest analogy in the slow-spreading mid-Atlantic ridge,
106 where magma chambers have been identified in the crust (MacGregor et al., 1998;
107 Heinson et al., 2000), and Iceland (e.g. Miensopust et al., 2014). The aim of our MT
108 studies was to image magma in the sub-surface, as an aid to understanding the
109 processes involved in dyke intrusion and late-stage continental crustal extension. MT
110 is ideally suited to this, for two main reasons. First, magma and partial melt have low
111 electrical resistivity, typically orders of magnitude lower than that of their host rock,
112 providing a good resistivity contrast. Second, MT is more sensitive to low resistivity
113 than high resistivity material. One of our MT profiles, about 50 km long, crossed the
114 axis of the Dabbahu magmatic segment, just to the north of the AVC. For comparison,
115 we also collected data along a ~45 km long profile across the adjacent currently
116 inactive Hararo segment to the south. We refer to these as the Dabbahu and Hararo
117 profiles, respectively. The third profile passed to the west of the Dabbahu volcano at
118 the northern end of the Dabbahu segment, and was oblique to the rift axis of the
119 magmatic segment; this is known as the Teru profile, since it runs close to the village
120 of Teru. It was 22.5 km long, with a slightly coarser site spacing than the other two.
121 The locations of the sites making up the three profiles are shown on Figure 2, along
122 with those of the volcanic and eruptive centres providing petrological information on
123 magma composition used to constrain its resistivity.

124
125 Desissa et al. (2013; hereafter Paper 1) modelled the Dabbahu profile data and found
126 low resistivities consistent with large quantities of partial melt, both in the crust and
127 underlying mantle. These MT data were collected 2 months after the intrusion of the
128 8th dyke in the sequence and another 2 months before the 9th. The model has a mid-
129 crustal conductor beneath the rift axis, with its top surface at about 5 km, but
130 minimum resistivity in the range 10-15 km. Conservative estimates of melt volumes
131 contained within it (Paper 1) are 25 km³, an order of magnitude larger than the
132 amount injected in the current rifting episode. Thus although its depth is consistent
133 with the inferred dyke source, its large volume is inconsistent with only short-term
134 storage. The model has a more extensive, Moho-straddling conductor to the west of
135 the rifted zone, where the Badi volcano projects onto the profile, containing ~500 km³
136 of melt. This deeper conductor is a good candidate to represent the long-term sub-
137 crustal magma storage required to satisfy the geochemical data (Ferguson et al.,
138 2013).

139
140 In section 2, we describe the data acquisition and processing, which leads to the
141 conclusion that the data along each of the three profiles are broadly consistent with a
142 two-dimensional (2D) sub-surface resistivity distribution. The 2D models for each of
143 the profiles are compared in section 3, and we discuss their interpretation in section 4.
144 Our conclusions are summarised in section 5.

145 146 **2. The magnetotelluric method**

147
148 The MT method is a passive source geophysical technique which involves measuring
149 the time-varying horizontal components of electromagnetic fields induced in the sub-

150 surface by the changing external magnetic field. Details of the method and associated
151 practicalities are given in text books such as Simpson and Bahr (2005) and Chave and
152 Jones (2012). The electric field was determined from the voltages and distances
153 (approximately 100m) between pairs of non-polarisable Pb-PbCl electrodes accurately
154 orientated in the magnetic North-South and East-West directions, and the magnetic
155 field measured by Metronix MFS05 or MFS06 broad-band induction coils, again
156 accurately orientated North-South and East-West and precisely levelled. The
157 electrodes were buried in a salty bentonite mud mixture to maintain good electrical
158 contact with the earth in the arid environment of Afar, and the coils were buried to
159 reduce wind noise. The sensors were connected to a pre-amplifier, and the data then
160 transferred to a digitising and recording unit which also allowed real-time data quality
161 control checks and preliminary processing to be performed, comprising a SPAM Mk3
162 (Ritter et al, 1998) or Mk 4 system. The equipment usually recorded for 1-2 days at
163 each site. At most sites, we also deployed transient electromagnetic (TEM) equipment
164 which monitors the resistivity of the very shallow sub-surface with a controlled
165 source, keeping the MT and TEM centres co-located as closely as possible to ensure
166 the two methods are probing the same lithologies. We used a Geonics PROTEM
167 system with source loop of 100×100 m (similar to the MT electrode separation) and
168 effective receiver loop size of 31.4 m^2 . The time rate of decay of magnetic flux was
169 recorded over integration times from 0.25 to 120 s. The majority of our sites were
170 accessed by four-wheel drive vehicles, but those over and to the east of the rifted zone
171 on the Dabbahu profile were installed using a helicopter owing to the rugged
172 topography. Much of the surface cover in the region is competent rock and therefore
173 unsuitable for burying coils and electrodes, but from SPOT satellite imagery we were
174 able to identify suitable sites in advance, with patches of shallow sand and/or
175 sedimentary cover of ~ 100 m diameter or more, and away from rapid changes in
176 topography as far as possible.

177
178 The MT data were robustly processed in the frequency domain using the algorithm of
179 Chave and Thomson (1989) to obtain the so-called ‘impedance tensor’ embodying the
180 sub-surface resistivity information. Short period ($< 7.8 \times 10^{-3}$ s) data collected with the
181 Metronix MFS05 induction coils were noisy, and have been excluded, but good
182 quality data up to 1.2×10^{-4} s period are available at many sites on the Hararo and
183 Teru profiles. At some sites the longest periods recoverable were only of order 100 s,
184 but at many sites we have impedance tensor estimates at periods longer than 1000 s.
185 We assessed whether the data along each profile were compatible with a 2D Earth
186 using the ‘strike’ algorithm of McNeice and Jones (2001). This solves simultaneously
187 for the geoelectrical strike direction (constant for all sites and periods), and
188 parameters characterising the effect of small-scale shallow heterogeneities which
189 cause non-inductive, or galvanic, effects in the data, also known as distortion, based
190 on Groom-Bailey (GB) decomposition of the impedance tensor (Groom and Bailey,
191 1989).

192
193 The system of equations used to determine the distortion model parameters and
194 geoelectrical strike direction is underdetermined, but can be fully resolved from the
195 TEM data. The ‘static shift’ manifests itself as a period-independent vertical offset
196 between the TE and TM mode apparent resistivity (the square of the relevant
197 impedance tensor element amplitude). The curves should coincide at periods shorter
198 than those penetrating the distorting region; however, even if they do, both may both
199 be shifted by an equal amount. Failure to correct for static shift will lead to erroneous

200 models. Sternberg et al. (1988) show how suitably scaled TEM decay curves can be
201 overlain on apparent resistivity curves to resolve static shift, since the two should
202 coincide in their region of overlap. Examples from this study are shown in Figure 3,
203 indicating that although often successful (Figure 3(a)), including identifying a static
204 shift even though both mode apparent resistivities agree at short period (Figure 3(b)),
205 on other occasions either there is insufficient period overlap to allow a static shift to
206 be determined reliably (Figure 3(c)) or the two cannot be brought into agreement
207 (Figure 3(d)). Site 812 in Fig 3(d) may be exhibiting distortion due to high electrode
208 contact resistance (e.g. Ferguson, 2012).

209
210 The goodness-of-fit of the data to the distortion model indicates whether the 2D
211 assumption is adequate. Misfits with the optimum strike direction for the three
212 profiles considered here (Figure 2) are given in Table 1 and Figure S2 of Paper 1, both
213 overall and for each site along the profile. There are some subtle trends in preferred
214 strike as a function of period (and hence depth), which probably indicate a number of
215 tectonic influences on the sub-surface structure, and possibly anisotropy effects.
216 However, at most sites and periods, the misfit is below the value of 2 usually taken as
217 indicating an acceptable fit to a 2D model.

218
219 Over a 2D Earth when the coordinate system is aligned with the geoelectric strike,
220 only the off-diagonal impedance tensor elements are non-zero; they define two
221 independent modes of induction known as the transverse electric (TE) and transverse
222 magnetic (TM) modes, corresponding to electric currents flowing parallel and
223 perpendicular to geoelectrical strike, respectively. The user must assign the
224 impedance tensor elements to either the TE or TM mode, using geological or other
225 information, since there is a 90° ambiguity. It is also useful to ascertain how well the
226 strike direction is determined (for example, whether the distortion model fit is
227 significantly worse for other assumed strike directions). The geoelectrical strike
228 values quoted below, and the broad consistency with two-dimensionality, are based on
229 the ‘strike’ algorithm, but were investigated by other methods, including phase tensor
230 analysis (Caldwell et al., 2004), which is useful since the phase tensor is unaffected by
231 static shift, GB decomposition applied to each site and period individually, and
232 subsets of the data along each profile simultaneously, and the general decomposition
233 technique of Council *et al.*(1986). The geoelectrical strike for the Dabbahu profile is
234 340°, consistent with the strike of the rift axis; likewise, the Hararo profile strike of
235 330° also matches the slightly more westerly orientation of that segment axis (in both
236 cases, the alternative perpendicular strike direction was ruled out on geological
237 grounds). Thus both cross-rift profiles are essentially perpendicular to strike, the
238 optimum arrangement for 2D modelling, with structure assumed invariant in the
239 along-strike direction. For the Teru profile, the best-fitting strike directions are 316°
240 or 046°, and thus the profile is not optimally orientated. We assumed a direction of
241 316°, closest to the rift axis orientation. However, the geoelectrical strike angle for
242 this profile is considerably less well-defined. For the three most northerly sites, the
243 data curves for the two modes at each site are very similar, and rotation has little
244 effect on the size of the diagonal impedance tensor elements (i.e. the strike is
245 undefined) or the fit to the distortion model. Also, for this profile only, different
246 methods for determining strike angle give rather different values.

247
248 Finally, we used the ρ^+ algorithm (Parker and Booker, 1996) to perform a consistency
249 check on the distortion- (including static shift-) corrected data assigned to their TE

250 and TM modes, as recommended by Jones and Ferguson (2001). The resulting Hararo
251 mid-segment and Teru profile data are shown in Figures 4 and 5 respectively; those
252 for the Dabbahu mid-segment profile were shown in Paper 1 (Figure 2). They are
253 presented as pseudo-sections of apparent resistivity and phase (lag between electric
254 and magnetic fields) as a function of period, which acts as a depth proxy. Apparent
255 resistivity increases or decreases with period as sub-surface resistivity increases or
256 decreases with depth, and phase less or greater than 45° indicates resistivity
257 increasing or decreasing with depth, respectively; the phase responds to resistivity
258 changes with depth at shorter periods than apparent resistivity. Thus both apparent
259 resistivity and phase data for the profiles crossing the magmatic segments indicate
260 two conductive zones in the sub-surface. The apparent resistivity lows are most
261 prominent at periods of about 0.1-1s and then 100-1000s. The low, decreasing phases
262 at the longest periods show the data detect a base to the deeper conductor. The
263 dominant feature of the Teru profile apparent resistivities is the extensive zone of very
264 low values (minimum $0.82 \Omega\text{m}$) at the northern end of the profile, close to the
265 Dabbahu volcano, starting from periods of about 0.1s. This severely restricts the depth
266 to which the data sample, although again the phase decrease with period at the longest
267 periods suggests the base of this conductor is sensed. In the next section, modelling
268 with 2D inversion confirms these deductions, and enables more quantitative
269 inferences on the sub-surface resistivity distribution to be made.

270
271

272 **3. Modelling**

273

274 For 2D modelling, we use the rebocc algorithm of Siripunvaraporn and Egbert (2000),
275 a regularised inversion approach which minimises a combination of the misfit
276 between the data and their predictions by the model and a measure of the amount of
277 structure in the model. Misfit is calculated in a weighted root-mean-square (RMS)
278 sense, i.e. the expected value is 1. However, values significantly above 1 may still be
279 regarded as an adequate fit, to allow for 3D and non-inductive effects in the data.
280 Inversion is usually undertaken with a specified data error floor. The error floor can
281 be different for the apparent resistivities and phases, recognising that static shift only
282 affects apparent resistivity, or for the TE and TM modes, since the TM mode is less
283 susceptible to 3D effects when, as here, it is expected to be associated with conductive
284 features. We used an error floor of 10% throughout; altering it has little effect on the
285 models obtained or the data predictions, though the RMS misfits change because of
286 the re-scaling of error bars. The model space, parameterised into blocks of constant
287 resistivity, is much larger than the area beneath the profiles, and extends to depths
288 well beyond the penetration of the data, to allow the boundary conditions appropriate
289 for this diffusion problem to be satisfied, using guidelines formulated by Weaver
290 (1994). The first layer was 10 m thick, and layer thicknesses increased by a factor 1.2-
291 1.5 to give a total model depth of about 130 km. The cells were typically 500 m wide
292 beneath and just beyond the edges of the profile for the Dabbahu and Hararo profiles,
293 and 1 km for the Teru profile where the site spacing was larger. We present the
294 models to a depth of 35 km for the cross-rift profiles (slightly less than the resolution
295 depth of about 40 km for the Dabbahu profile inferred from sensitivity tests in Paper
296 1), and 20 km for the shorter Teru profile where the very low resistivity at the
297 northern end restricts the penetration of the data. The models are shown in Figure 6,
298 and the data fits on a site-by-site basis in Figures 7, 8 and 10.

299

300 Despite the data providing a good fit to 2D distortion models, it is impossible to find
301 2D models adequately fitting some aspects of the data. Particular difficulties are
302 presented by large changes in longer period TE mode apparent resistivities over short
303 distances, most notably on the Dabbahu profile, and to a lesser extent between sites
304 915, 916 and 917, and between 907 and 110, on the Hararo profile (Figure 7), which
305 are inconsistent with the 2D assumption. After excluding some data inconsistent with
306 the 2D assumption and some particularly noisy data (as discussed in the
307 Supplementary Material of Paper 1), the resulting best-fitting Dabbahu profile model
308 has an RMS misfit of 2.3; that for the Hararo profile was 2.4. Most of the gross
309 features of the data are well modelled, for instance, the data curves for the two modes
310 separate at the right period, the magnitude of the split in the phases between the two
311 modes is reasonably well-reproduced at most sites, and the TM mode predictions are
312 usually good. The Teru profile model suffers less from these modelling issues, since
313 the TE mode apparent resistivity at longer periods varies slowly and consistently
314 along the profile, although it is slightly under-predicted at site 101 (Figure 8), which
315 contributes most to the overall RMS misfit of 1.7. The Teru profile sites have
316 progressively lower apparent resistivities at the longest periods moving north along
317 the profile, which are well-matched by progressively lower model resistivities
318 (reaching a minimum of $0.08 \Omega\text{m}$, considerably less than that of seawater at average
319 salinity and temperature) over a greater vertical extent. However, the rapid drop in
320 phase at the longest periods is not well reproduced, especially in the TM mode. This is
321 most likely because regularised inversion tends to discriminate against the rapid
322 increase in resistivity with depth it implies. There is also a hint of this in the TM mode
323 apparent resistivities since the data curves level out or even have a slight upturn at the
324 longest periods (Figure 8). The resistivity structure of the southern-most end of the
325 model is similar to that of the Dabbahu profile model where the Teru profile projects
326 on to it.

327
328 All three models have a thin, variable thickness (500m to 2 km) conducting layer
329 close to, and sometimes reaching, the surface, embedded within otherwise resistive
330 material, generally approaching $1000 \Omega\text{m}$, though typically an order of magnitude
331 lower to the east of the rift axis on the Dabbahu profile. The high resistivity unit is
332 likely to represent basaltic crust, whereas the conductive layer can be explained by
333 large volumes of saline fluids/evaporite in recent sediments that have been extensively
334 faulted, fractured and intruded, or highly weathered basalt (found at shallow depths in
335 boreholes drilled for ground water). Field et al. (2012) find evidence for fractionation
336 in the presence of brines in samples collected from the Dabbahu volcano and the
337 AVC. There are large, economic salt deposits at Afdera and Dallol, to the north of
338 Dabbahu, which Talbot (2008), Chernet (2012) and Atnafu et al. (2015) suggest result
339 from repeated marine flooding (but see Hovland et al. (2008), who argue for a largely
340 hydrothermal origin). Delays in crustal receiver functions across the area are
341 consistent with substantial thicknesses of sediments (Hammond et al., 2011). At
342 Dubti, to the south of the Hararo profile, boreholes found up to 1500m of lacustrine
343 sediments (Abbate et al., 1995), or sediments interspersed with fissure basalts
344 (Battistelli et al., 2002) as modelled by Bridges et al. (2012) to satisfy gravity and
345 magnetic data.

346
347 Resistivity is significantly reduced in parts of the lower crust in the cross-rift profiles,
348 whose base is ~ 22 km beneath the Dabbahu segment, and less well constrained at
349 about 22-26 km beneath the Hararo segment (Hammond et al., 2011). This strongly

350 suggests the presence of substantial amounts of partial melt. The Dabbahu profile
351 model has two distinct lower crustal conductors, one centred on the rift axis, the other
352 with a deeper (~ 10 km) top surface extending into the mantle to the west of the rift
353 axis, where the Badi volcano projects from a few kilometres north onto the profile.
354 The Hararo profile has a single conductivity maximum in the lower crust, about 15
355 km to the east of the rift axis (which is at site 913) and at a depth of about 20 km, but
356 the maximum is less pronounced compared to those on the Dabbahu profile and the
357 whole of the lower crust is conductive.

358
359 The most striking feature of the Teru profile model is the extremely low resistivities
360 inferred in the crust near the Dabbahu volcano (the white region in Figure 6, where
361 $\log_{10}\rho < 0.1$ or $\rho < 1.26 \Omega\text{m}$). Note that this feature is relatively unaffected by the
362 choice of geoelectrical strike direction assumed – in fact, the model beneath the most
363 northerly three sites is very similar in the extreme case of a 90° change to assumed
364 geoelectrical strike angle (i.e. when the TE and TM modes are swapped). Since
365 regularised inversion tends to smear structure, especially vertically, and discriminate
366 against rapid changes in resistivity, it is difficult to be precise about the vertical
367 variations in resistivity, apart from the depth to the top surface of the conductor. The
368 data sense a decrease in resistivity at the longest periods, so it is not plausible to
369 distribute the conductive material over greater depths than in the model of Figure 6.
370 Forcing a resistive ($1000 \Omega\text{m}$) mantle (starting at ~22 km depth, the crustal thickness
371 there; Hammond et al, 2011) slightly reduces the data misfit, primarily by fitting the
372 longest period data at sites 102-104 better. The model is unphysical – it has a
373 conductive zone (minimum resistivity of only $0.03 \Omega\text{m}$) beginning at about 3 km
374 depth beneath site 104, broadening to ~10 km wide with depth, terminating abruptly
375 at the Moho, which would be an implausible melt distribution. However, it does
376 suggest that a model with a more rapid depth termination of the conductor than is
377 obtained by unconstrained regularised inversion would be more appropriate. The
378 conductance also depends on the resistivity structure, with a maximum of 98 kS,
379 equivalent to about 20 km of seawater, for the model of Figure 6, but 265 kS when the
380 conductor is confined to the crust. The high conductivities encountered and relatively
381 short profile mean that depth resolution is limited, so although the data sense some
382 deeper structure, its nature is extremely uncertain; we therefore limit the depth extent
383 to which this profile is displayed in Figure 6 to 20 km, but caution that the details of
384 the structure shown even towards the base of the crust are ambiguous. Similarly, the
385 structure to the north of site 104 is poorly constrained owing to the absence of sites
386 there.

387

388 **4. Interpretation**

389

390 The 2D resistivity models can be used to infer minimum amounts of magma in the
391 sub-surface. The low resistivity values indicate well-connected melt, implying that the
392 parallel conducting pathways (Roberts and Tyburczy, 1999) or Hashin-Shtrikman
393 upper bound (Hashin and Shtrikman, 1962) model is appropriate to infer melt
394 fractions from bulk resistivity. For both models, the result depends only on melt
395 fraction and melt resistivity, being virtually insensitive to host rock resistivity.
396 Minimum melt percentages derived here are obtained from the parallel pathways
397 model, in which current flows parallel to sheets of either melt or solid whose relative
398 thicknesses are given by the volume fraction. The lower crustal basaltic melt
399 resistivity estimated from geochemical analysis of samples from Dabbahu, Badi and

400 the AVC (Field et al., 2012; Ferguson et al., 2013) at ~20 km depth using the web-
401 based tool Sigmelts (Pommier and Le Trong, 2011) was 0.28 Ωm (Paper 1). In Paper
402 1, we noted that given the range of geochemical uncertainties, SiO_2 content has the
403 biggest influence, allowing melt resistivity values more than a factor of two different
404 from that calculated from the mean. The conductor depth beneath the Hararo profile is
405 similar; lacking samples from there, we assumed the same melt resistivity value when
406 interpreting that profile.

407
408 In the model of the Dabbahu profile (Figure 6), resistivity contours for the two main
409 conductors were roughly circular, and hence so were inferred melt fraction contours,
410 ignoring depth (i.e. pressure and temperature) changes in melt resistivity. For the
411 Moho-straddling conductor, converting resistivity to melt fraction using the parallel
412 conducting pathways model (to get the minimum amount) indicated it decreased
413 approximately linearly from a maximum of 13% to 3% at 13 km distance. The
414 assumption of 2D modelling is that structure continues unchanged in the along-strike
415 direction, but we adopted spherical symmetry to terminate the body. Integrating the
416 linearly varying melt fraction over a sphere of radius 13 km (neglecting melt at lower
417 fractions), it contains a total melt volume of approximately 500 km^3 . The shallower
418 conductor beneath the rift axis contains approximately 25 km^3 melt, accounting for
419 the higher melt resistivity owing to its shallower depth and lower temperature.
420 Beneath the Hararo profile, the minimum resistivity value in the model of Figure 6
421 implies 5.3% melt. In this case, the approximately circular contours of the main
422 conductor are well fit by an exponential decay in melt fraction with distance, given by
423 $f = 0.0527 \exp(-0.105r)$, where f is melt fraction and r is distance (in km) from the
424 centre. Integrating out to 5 km distance, where there is about 3% partial melt (again,
425 neglecting melt at lower fractions), gives a total melt volume of 20 km^3 . Melt beneath
426 the Hararo segment is present throughout the lower crust, making the spherical
427 symmetry assumption less reliable. In fact, this estimate neglects melt to the west of
428 the rift axis, including areas where the amount of melt rises to above 3% again.
429 However, the neglected melt will not bring the total to more than a fraction of that
430 inferred beneath the Dabbahu segment.

431
432 Although Paper 1 provided compelling evidence for large quantities of magma in the
433 lower crust and mantle where the Badi volcano projects onto the Dabbahu profile,
434 regularised modelling does not constrain how this magma is distributed. Geochemical
435 arguments favour mantle magma concentrated into sills, rather than one large
436 chamber (e.g. Maclennan et al., 2001). Such a model would not be produced by our
437 inversion scheme, since regularisation would discriminate against the associated rapid
438 vertical variations in resistivity. However, by dividing the Moho-straddling conductor
439 in the best-fitting regularised model into a series of resistive bands separated by
440 conducting layers (representing the sills) and re-running the inversion, we have
441 produced a sill-like model (Figure 9). The horizontal discretisation of our model space
442 represents the resolution of the data, so there are relatively few bands and the deeper
443 ones are thicker. The resistive bands are compensated for by even lower resistivity in
444 the conducting layers to maintain the overall conductance. The vertical breaks in the
445 resistive material between the sills are not necessary to fit the data, but are introduced
446 to provide a pathway for the melt to flow upwards, as in geochemical models. It
447 would be possible to have a more realistic model with more, thinner bands; the model
448 of Figure 9 was produced to illustrate that sill-like models are also a feasible
449 explanation of our data. In general, the resistivity of the resistive background is

450 controlled by the TM mode data, whilst that of the conductive sills by the TE mode
451 data (Berdichevsky, 1999). In this case, we imposed a modest resistivity (100 Ωm) on
452 the layers between the sills, and allowed the resistivity of the remaining blocks to
453 vary, providing an equally good fit to the TE mode data (Figure 10). The slight
454 degradation in the fit to the long period TM mode data could be overcome by
455 adjusting the resistive structure between the sills. The decrease of the minimum
456 resistivity with depth could reflect the decrease in melt resistivity with depth, a
457 variation we have again neglected when estimating melt fractions from bulk resistivity
458 in this sill-like model. In this case, the minimum resistivity is 1.89 Ωm , a little more
459 than half that of the model of Paper 1, implying >22% partial melt. Again, we
460 calculated volumes assuming spherical symmetry, and calculated volumes in disks
461 with > 3% melt, ignoring regions with lower melt fractions. Similarly, we treated the
462 melt fraction as linearly increasing through the disk to its maximum value in each
463 case. The result is a slightly higher minimum melt volume ($\sim 600 \text{ km}^3$) than when the
464 conductor is a single body ($\sim 500 \text{ km}^3$; Paper 1).

465
466 Seismic evidence supports the existence of significant amounts of melt in the crust
467 and mantle in our study region. There are broad, pronounced low velocity features
468 over the area of our profiles from both surface wave up to 12 s period (Guidarelli et
469 al., 2011) and P_n (Stork et al., 2013) studies. High upper crustal seismic anisotropy
470 values are attributed to melt pockets in cracks oriented parallel to the rift segment
471 axes (Keir et al., 2011). Through a combination of numerical modelling and
472 geochemistry, Armitage et al. (2015) provide strong evidence that lithospheric melt is
473 necessary to explain features of the seismic data. Crustal receiver functions typically
474 have high V_p/V_s values (Hammond et al., 2011). Receiver function studies suggest a
475 difference in crustal structure either side of the current rift axis (Hammond et al.,
476 2011), associated with the migration of the Afar triple junction and the Red Sea rift
477 axis over time. To its west, the crust is thinner and contains more partial melt (higher
478 V_p/V_s); to its east, it is thicker and retains a more continental-like signature, even
479 though it is still stretched and intruded. Our Dabbahu segment model, whose profile
480 lies on a short segment of Hammond et al.'s (2011) > 300 km-long profile C-C', also
481 has a difference in structure either side of the rift axis, with no indication of
482 significant amounts of melt to its east, consistent with the seismic interpretation. Our
483 Hararo profile is between their profiles B-B' and C-C'. Their more southerly B-B'
484 profile has partial melt distributed across both sides of the rift axis ($V_p/V_s > 2.0$),
485 again consistent with our MT model (in fact, our more conductive region is to the east
486 of the axis). B-B' is to the south of the magmatic segment, so the comparison may not
487 be entirely appropriate, but we note that multiples from which the receiver functions
488 are calculated are sensitive to a region of approximately 25 km diameter from the
489 seismic station, which is less than the distance of our Hararo profile from B-B'. In
490 striking agreement with our results, Belachew (2012) finds, from P- and S-wave
491 tomographic inversion of ~ 37000 local earthquake phases from ~ 1300 earthquakes
492 (with hypocentre relocation), two pronounced low velocity zones, beneath Dabbahu
493 volcano and to the west of the AVC, extending to depths of 28 km (the maximum in
494 the tomography model). The zone to the west of the AVC is at the same distance from
495 the rift axis as our mantle-straddling conductor on the Dabbahu and Teru profiles
496 from depths of 18 km, but closer to the axis at shallower depths, even extending both
497 sides of it below 8 km depth. Resolution is not sufficiently good to distinguish
498 unambiguously the continuity or otherwise between the low velocity zones, but there
499 is a suggestion that the zones beneath Dabbahu and to the west of the AVC are

500 connected along-axis beneath 13 km. Note that the Dabbahu low velocity zone
501 extends into the mantle (in fact, to 28 km, the maximum depth of the tomography
502 model), in better agreement with the regularised model shown in Figure 6 than that in
503 which we impose a resistive mantle. Converting a 0.2 km/s V_p reduction to a
504 minimum of 1-4% melt (Schmeling, 1985; Magde, 2000), Belachew (2012) infers at
505 least 7-12% partial melt to explain these velocity anomalies. He also finds low V_p
506 velocities in the lower crust in the area of our Hararo profile; they are particularly
507 pronounced around 18 km depth and much closer to normal by 23 km depth.
508 However, there is no evidence from the tomography results of the low velocities being
509 concentrated to the east of the rift axis there.

510
511 Our Hararo profile is just to the north of the site of the Tendaho geothermal prospect,
512 which has and continues to be investigated by a number of geophysical and other
513 methods. Here, structure of the top 5 km is of particular interest, and a series of MT
514 studies have collected data to periods of up to 1000 s, showing crustal resistivities at
515 least as low as in our Hararo profile model (Didana et al., 2014). The almost
516 ubiquitous near surface conductor in our models is also present. A sub-vertical
517 conductive feature (Kalberkamp, 2009; Didana et al., 2014) potentially mapped a
518 feed for the shallow heat reservoir, which achieved temperatures of 300°C at 300 m
519 depth (Aqater, 1996). Magnetic and gravity data have been collected to seek
520 confirmation that this is a fracture zone that could form a potential pathway for
521 hydrothermal fluids feeding the shallow reservoir (Lemma and Hailu, 2006).

522
523 The most striking feature of the Teru profile model (left-most model in Figure 6) is
524 the extremely conductive zone at its northern end. From petrological, seismic and
525 remote sensing information, Field et al. (2012) inferred a substantial and long-lived
526 magma storage region between approximately 1.5 and 5.5 km depth beneath the
527 active Dabbahu volcano, with sills the most favoured geometry. The maximum
528 conductivity in our model is at ~6.5 km depth, and we are unable to fit the data with a
529 conductor confined to the top 5 km or so. The largest percentage P-wave velocity
530 reduction beneath Dabbahu in the tomography model of Belachew (2012) occurs at 8
531 km. However, although the first-order agreement is good, there are several challenges
532 to a more detailed interpretation. The average resistivity in the crust near Dabbahu
533 volcano is of order 0.5 Ωm . This is typical of or lower than values for pure basaltic
534 melt of most compositions at crustal depths and temperatures (Pommier and Le
535 Trong, 2011). The wide range of erupted products from the Dabbahu volcano implies
536 considerable variation in melt composition and conditions. For instance, parent
537 basaltic melt water content is 0.4-0.5 weight %; however, the recently erupted, much
538 more evolved, lavas have water content up to 5.8 wt % (Field et al., 2012). The very
539 evolved rhyolites (pantellerite and commendite) comprise less than 5% of the erupted
540 products, but require ~80% crystallisation in the top 6 km of the crust (Field et al.,
541 2013). More generally, we might expect to encounter changing melt composition, and
542 hence resistivity, associated with changing melt fractions as magma cools and
543 crystallises. Melt resistivity is strongly dependent on SiO_2 and water content over the
544 range of permissible values, which could encompass values of 47-70 % and 0.4-8 %
545 respectively (Field et al., 2012, 2013); this will change melt resistivity by more than
546 an order of magnitude (Pommier and Le Trong, 2011; Laumonier et al., 2015). Even
547 the possible 1% change in Na_2O and range of pressures and temperatures encountered
548 will have a noticeable impact. Modelling the possible melt supply and evolution, and
549 associated variations in its resistivity, is beyond the scope of the present study, and in

550 any case is subject to a great degree of uncertainty. Whatever compositions and hence
551 melt resistivities are assumed, and regardless of the ambiguities associated with the
552 MT model, it indicates that there is a resolvable magma reservoir of (close to) pure
553 melt associated with the volcano. A typical evolved composition from melt inclusions
554 hosted in feldspars (Field et al., 2012) has $\text{SiO}_2 = 72.1 \pm 1.4$, $\text{Na}_2\text{O} = 5.9 \pm 0.41$ (both
555 weight %, and 1 standard deviation uncertainties), $P = 250$ MPa, $T = 1200^\circ\text{C}$;
556 Pommier and Le Trong (2011) predict a melt resistivity of $0.16 \Omega\text{m}$ if we assume their
557 highest (5.8%) H_2O content, lower than for basaltic melt but markedly higher than the
558 lowest resistivity seen in the conductor. Laumonier et al.'s (2015) investigation of the
559 conductivity of a silica-rich melt has found values of typically half an order-of-
560 magnitude higher than those of Pommier and Le Trong (2011), dependent on
561 temperature and water content (their Fig. 9). Hence we have assumed a melt
562 resistivity of $0.1 \Omega\text{m}$, giving the melt percentages shown in Figure 11. The melt
563 region extends to below the 15 km depth plotted, but is ignored in our estimates of the
564 melt volume since resolution there is poorer. We also assume the magma body is
565 symmetric about site 104, using the better constrained structure to the south to define
566 a set of nested cylinders with decreasing amounts of melt with lateral distance from
567 site 104. These assumptions, and the limitations from having interpreted a particular
568 2D model, mean that the melt volume inferred is highly uncertain. Note that these
569 estimates are also conservative since they are based on the parallel conducting
570 pathway model, which is appropriate when melt is arranged in oriented melt pockets,
571 i.e. the sub-surface is anisotropic, but there are virtually no differences between the
572 phases of the two modes in the northern Teru line data that are normally taken as an
573 indication of electrical anisotropy. If we treat the amount of melt in each cylinder or
574 annulus as constant at the mid-value of the range, we get a total indicative melt
575 volume of 80 km^3 , about three times that in the conductor directly beneath the
576 Dabbahu segment rift axis, less than the total eruptive volume from Dabbahu (> 115
577 km^3 ; Field et al., 2013), and substantially less than beneath the deeper conductor close
578 to the Badi volcano (500 km^3 ; Paper 1).

579
580 Ferguson et al. (2013) analysed both on- and off-axis lavas from the Dabbahu
581 segment near our profile (from the AVC and Badi, respectively; see locations on Fig.
582 2), and found them to have different chemical signatures. The on-axis lavas were
583 extracted rapidly and/or without chemical interaction, whereas the off-axis lavas re-
584 equilibrated in the upper mantle. Our off-axis mantle magma reservoir is consistent
585 with Ferguson et al.'s (2013) re-equilibration zone, and the lack of a deeper conductor
586 beneath the axial rifting region supports rapid extraction there. In the lower crust
587 beneath the Dabbahu profile, there is a conducting pathway between the off- and on-
588 axis conductors (e.g. Paper 1, Fig. 3), albeit with a slight resistivity increase.
589 However, breaking the conducting pathway between them (in both the regularised and
590 sill-like model) does not noticeably alter the fit to the data, so we cannot distinguish
591 between separate and connected magma sources. The possibility of a rift jump to
592 accommodate the eastward migration of the Red Sea rift axis over time is suggested
593 by the two partial melt locations beneath the Dabbahu profile. Consistent with the
594 conclusions of Ferguson et al., (2013), Medynski et al. (2015) find that the off-axis
595 reservoir has not supplied the recent dykes, but that it was the main focus of magma
596 accumulation prior to 15 ka, and has been regularly supplied since. They suggest that
597 the current rift axis has been active for the last 30 kyr, but its magma supply has
598 diminished over the last 20 kyr. Daniels et al. (2014) drew a similar conclusion on the
599 basis of numerical modelling of the heat flow equation: more than one locus of

600 heating is required, to prevent significant localised ductile stretching that would
601 otherwise by now have weakened and thinned the crust by far more than that
602 observed. As already noted, the asymmetric seismic velocity and resistivity structure
603 either side of the current rift axis is consistent with it having migrated. Although much
604 of the lower crust is conductive between the projection of the Badi and the Dabbahu
605 volcanoes onto our Teru profile, we expect on the basis of the geochemistry that the
606 two are separate. Thus we have imaged four separate magma/partial melt regions –
607 beneath the rift axis, the Badi and Dabbahu volcanoes on the active Dabbahu segment,
608 and concentrated to the east of the rift axis beneath the inactive Hararo segment – with
609 a conservative combined melt volume of $> 600 \text{ km}^3$, using the differences in
610 composition, temperature and depth of the sources to provide the most reliable melt
611 resistivities from which these volumes were inferred.

612
613 The Afar region is thought to be a region of incipient slow sea-floor spreading, with
614 magmatic processes far more important than tectonic ones. To what extent crust being
615 generated there is ocean-like, whether there is any residual influence from the mantle
616 plume(s) that impinged on the region $\sim 45 \text{ Ma}$, and how and where melting occurs,
617 remain matters of debate (e.g. Armitage et al., 2015). The limited depth extents of our
618 profiles mean we are unable to contribute to the discussion on melting depths and
619 processes, and symmetry or otherwise of melt regions generated by mantle upwelling
620 or buoyancy forces (especially as the crust beneath our profiles is much thicker than
621 beneath mid-ocean ridges), but we can compare our results with shallower images,
622 both electrical and seismic, of mid-ocean ridges (at a variety of spreading rates) to
623 assess the extent to which they have features in common, bearing in mind that mid-
624 ocean ridge environments are profoundly affected by hydrothermal circulation.

625
626 Beneath two profiles crossing the fast-spreading East Pacific Rise (EPR), sub-vertical
627 conductors in the mantle have been interpreted to contain high melt concentrations
628 (Baba et al., 2006; Key et al., 2013). Baba et al. (2006) prefer an anisotropic model
629 with a flat resistive-conductive interface at about 60 km depth with a highly
630 conductive across-ridge conductor below, and a vertical current sheet in the ρ_{zz}
631 component beneath the ridge axis. Key et al. (2013) infer virtually no anisotropy
632 except for slight enhanced conductivity in the ρ_{zz} component to the east of the ridge in
633 the shallow mantle. In the more northerly location, the conductor was offset from the
634 rift axis at depth, it impinged on the base of the crust where there was a low seismic
635 velocity anomaly (Toomey et al., 2007), and it was interpreted as a porous melt
636 channel rapidly delivering magma to the crust (Key et al., 2013). In the part of Afar
637 we investigated, the highest mantle conductivities are also offset from the rift axes,
638 and the base of the crust and uppermost mantle are seismically slow (Guidarelli et al.,
639 2011; Stork et al., 2013); we lack the depth penetration to determine whether these
640 broad conductors become more laterally confined at depth. Magma is stored in the
641 crust in both axial and off-axis (4-8 km from the axis) locations beneath the EPR, in
642 the latter, in partially molten lower-crustal sills (Canales et al.; 2012); although there
643 was mixing between the two, lavas erupted off-axis had more variable composition
644 (Perfit et al., 1994). Beneath the Dabbahu segment, there is considerable along-axis
645 compositional variability (comparing lavas from the AVC and Dabbahu volcano), and
646 there is geochemical evidence against mixing between the axial and off-axis magmas
647 (which are further apart than at the EPR). Provisional 3D modelling (Hautot et al.,
648 2012) indicates axis-parallel continuity of the lower-crustal conductors in Afar, but
649 there are no associated surface eruptions. Similarly, at the intermediate spreading rate

650 Juan de Fuca ridge, an off-axis lower crustal melt lens (interpreted as a sill) a few
651 kilometres long in the ridge-parallel direction and a shallower axial magma chamber
652 were imaged by seismic reflection (Canales et al., 2009).

653

654 Studies of the slow-spreading mid-Atlantic ridge (MAR) have imaged transiently- or
655 fluctuatingly-supplied crustal magma chambers, with variability on timescales up to ~
656 2 Myr and over distances less than 80 km (e.g. Karson et al., 1987), but again
657 provided no evidence of substantial amounts of melt in the upper mantle. A multi-
658 technique study of the magmatically active Reykjanes Ridge indicated a transient
659 magma chamber in the crust, similar to those observed at faster spreading ridges (e.g.
660 Sinha et al., 1997). A seismic reflection survey of the Lucky Strike section of the
661 MAR indicated an axial magma chamber, with median valley faults continuing down
662 to or beneath the chamber (Singh et al., 2006). The width of the faulted region is
663 similar to that for Afar magmatic segments, but does not have the fault density
664 asymmetry about the rift axis observed over the Dabbahu segment (Rowland et al.,
665 2007) that our shallow sub-vertical conductor to the west of the rift axis (between
666 sites 807 and 811 in Fig. 9) is consistent with, nor does it have such a high fault
667 density. Also, Wright et al. (2006) estimate that normal faults only extend to a depth
668 of 2 km beneath the Dabbahu segment. Like Afar, both of these MAR areas are
669 possibly influenced by mantle plumes. In an unaffected area further south, Canales et
670 al. (2000) deduced up to 17% partial melt (if melt inclusions have large aspect ratios)
671 in the middle and lower crust beneath the ridge.

672

673 Comparing the volumes of magma available in our models to those intruding during a
674 dyking cycle (which happens every ~500 years) or required to build the full thickness
675 of the crust (rather than just intruding part of it as it is stretched and thinned) at the
676 far-field spreading rate indicates they contain sufficient for at least several tens of kyr
677 beneath the Dabbahu segment (the timescale over which MAR segments can change
678 from being magma-starved to magma-enriched; Canales et al., 2000). However, there
679 is doubt from the geochemical analyses as to whether the mid-segment axial magma
680 chamber is connected to the deeper off-axis one and/or to the one beneath the
681 Dabbahu volcano at the northern end of the segment, so we cannot rule out a transient
682 supply to the axial chamber. The inactivity on the Hararo segment, where there are
683 also notable volumes of magma in the deep crust, again displaced from the rift axis,
684 suggests this might be the case. However, InSAR data indicate that the Dabbahu
685 segment axial magma chamber barely inflated or deflated during the recent dyke
686 intrusions it sourced (Hamling et al., 2009). Thus the geometry and temporal
687 variability of the plumbing systems responsible for extrusive and intrusive volcanism
688 in the region remain uncertain.

689

690

691 **5. Conclusions**

692

693 We have presented MT data and 2D models from three profiles in the Afar region of
694 Ethiopia, two over and near the active Dabbahu magmatic segment, the other over the
695 currently inactive Hararo segment. The low resistivities encountered in the cross-
696 segment profiles suggest that there are significant amounts of magma and partial melt
697 beneath both segments, much more than is required to supply the recent dyke
698 intrusions and eruptions, and sufficient to build the crust at the far-field spreading rate
699 for of order a few tens of kyr. Inferred melt volumes are higher beneath the active

700 segment, and a substantial amount is in the mantle to the west of the rift axis.
701 However, there are still significant quantities of melt beneath the Hararo segment, but
702 in this case, more widely dispersed laterally and, depth-wise, mainly straddling the
703 Moho. Beneath the Dabbahu volcano, our model has resistivities so low as to indicate
704 pure melt in the shallow crust and implies a large melt volume. These inferences of
705 large quantities of melt and its location are broadly in agreement with conclusions
706 from seismological information, although the distribution and melt fractions are not
707 identical. Petrological analysis of samples from the Badi volcano to the west of the
708 Dabbahu rift axis and recent rift axis eruptions give melting depths of 75-100 km.
709 Badi samples are from magma that has re-equilibrated near the top of the mantle, in
710 agreement with the low resistivity body in our model, in contrast to those from axial
711 eruptions, which are transported quickly from their melting depth. This mantle melt
712 could as easily be contained in sills as in a single magma body. A summary cartoon of
713 the melt distribution is given in Figure 12. The lack of inflation and deflation
714 signatures associated with the recent series of dyke intrusions beneath the Dabbahu
715 segment suggests a continuous magma supply. However, InSAR results indicate that a
716 region to the south of the Dabbahu segment, between that and the Hararo segment, is
717 currently deflating, perhaps implying a lateral movement of magma to supply the
718 current dyking episode (T Wright, pers. comm., 2012). Our results indicate that there
719 is magma available there. Three-dimensional modelling of the data, including a few
720 sites to the north of the Hararo segment line not shown in Figure 2, may indicate
721 whether there could be a connection between the zones of partial melt beneath the
722 Dabbahu and Hararo segments.

723
724

725 **Acknowledgements**

726

727 This research has been supported financially by NERC (grant NE/E007147/1 and PhD
728 studentship for NEJ), the School of GeoSciences (MSc by Research MTEM Partial
729 Scholarship to MD), CNRS (funding for SH), and in-kind by equipment loans from
730 the NERC Geophysical Equipment Facility (GEFSC loans 855, 866 and 907), and the
731 Geophysical Instrument Pool Potsdam (part of GeoForschungsZentrum) through the
732 auspices of Oliver Ritter and Ulrich Kalberkamp (formerly of BGR, Hannover). The
733 Geophysical Observatory (part of the Institute for Geophysics, Space Science and
734 Astronomy), Addis Ababa University and the Geological Survey of Ethiopia are
735 thanked for extensive logistical support, as is Yohannes Lemma (Geological Survey
736 of Ethiopia) for help with the fieldwork. The Afar Regional Government enabled
737 access to the field area and provided significant practical assistance. Helicopter access
738 to the Dabbahu rift was ably and cheerfully provided by pilot Chris Stewart from
739 Everett Aviation (Kenya). SPOT imagery was provided to SH by CNES, France. We
740 also acknowledge discussions with and results in advance of publication from Afar
741 Rift Consortium colleagues and Project Partners, in the UK, Ethiopia, USA and New
742 Zealand. We thank the reviewers (Ian Ferguson and one anonymous) and the editor
743 David Ferguson for their constructive comments.

744

745 **References**

746

747 Abbate, E, Passerini, P and Zan, L, 1995 Strike-slip faults in a rift area: A transect in
748 the Afar triangle, East Africa, *Tectonophys.*, **241**, 67-97

749

750 Aizawa, K, et al, 2011. Temporal changes in electrical resistivity at Sakurajima
751 volcano from continuous magnetotelluric observations, *J. Volc.. Geotherm. Res.*, **199**,
752 165–175
753

754 Aquater, 1996, Tendaho geothermal project, final report, Ministry of Mines of
755 Ethiopia and Ministry of Foreign Affairs of Italy, San Lorenzo in Campo, Italy
756 (unpublished)
757

758 Armitage, J J, Ferguson, D J, Goes, S, Hammond, J O, Calais, E, Rychert, C A and
759 Harmon, N, 2015. Upper mantle temperature and the onset of extension and break-up
760 in Afar, Africa, *Earth Planet. Sci. Letts.*, **418**, 78-90
761

762 Atnafu, B, et al., 2015. Reading history from Afar, *Eos*, **96**,
763 doi:10.1029/2015EO022789
764

765 Ayele, A, *et al.*, 2009, September 2005 mega-dike emplacement in the Manda-
766 Harraro nascent oceanic rift (Afar depression), *Geophys. Res. Lett.*, **36**, L20306,
767 doi:10.1029/2009GL039605, 2009
768

769 Baba, K, Chave, A D, Evans, R L, Hirth, G and Mackie, R L, 2006. Mantle dynamics
770 beneath the East Pacific Rise at 17°S: Insights from the Mantle Electromagnetic and
771 Tomography (MELT) experiment, *J. Geophys. Res.*, **111**, B02101
772

773 Battistelli, A, *et al.*, 2002. Reservoir engineering assessment of Dubti geothermal
774 field, Northern Tendaho Rift, Ethiopia, *Geothermics*, **31**, 381-406,
775 doi:10.1016/S0375-6505(01)00039-6
776

777 Belachew, M, *et al.*, 2011, Comparison of dike intrusions in an incipient seafloor-
778 spreading segment in Afar, Ethiopia: Seismicity perspectives, *J. Geophys. Res.*, **116**,
779 B06405, doi:10.1029/2010JB007908
780

781 Belachew, M, 2012, Dynamics of dike intrusions and 3D velocity structure beneath an
782 incipient seafloor spreading center in Afar, Ethiopia, unpublished PhD thesis,
783 University of Rochester, USA
784

785 Berdichevsky, M N, 1999, Marginal notes on magnetotellurics, *Surv. Geophys.*, **20**,
786 341-375

787 Bologna, MS, Padilha, AL, Vitorelli, I and Padua, MB, 2011, Signatures of
788 continental collisions and magmatic activity in central Brazil as indicated by a
789 magnetotelluric profile across distinct tectonic provinces, *Precambr. Res.*, **185**, 55-64

790 Brasse, H and Eydam, D, 2008, Electrical conductivity beneath the Bolivian Orocline
791 and its relation to subduction processes at the South American continental margin, *J.*
792 *Geophys. Res.*, **113**, B07109, doi: 10.1029/2007JB005142
793

794 Bridges, D, Mickus, K, Gao, S, Abdelsalam, M and Alemu, A, 2012, Magnetic stripes
795 of a transitional continental rift in Afar, *Geology*, **40**, 1-4
796

797 Caldwell T G, Bibby H M and Brown C, 2004, The magnetotelluric phase tensor,
798 *Geophys. J. Int.*, **158**, 457-469
799

800 Canales, J P, Collins, J A, Escartín, J and Detrick, R S, 2000, Seismic structure across
801 the rift valley of the Mid-Atlantic Ridge at 23°20' (MARK area): Implications for
802 crustal accretion processes at slow-spreading ridges, *J. Geophys. Res.*, **105**, 28411-
803 28425
804

805 Canales, J P, *et al.*, 2009, Seismic reflection images of a near-axis melt sill
806 within the lower crust at the Juan de Fuca ridge, *Nature*, **460**, 89-94,
807 doi:10.1038/nature08095
808

809 Canales, J P, *et al.*, 2012. Network of off-axis melt bodies at the East Pacific Rise,
810 *Nature Geosci.*, **5**, 279-283, doi: 10.1038/ngeo1377

811 Chave, A and Jones, A G (editors), 2012, *The Magnetotelluric Method: Theory and*
812 *Practice*, Cambridge University Press, Cambridge, UK

813 Chave, A D and Thomson, D J, 1989, Some comments on magnetotelluric response
814 function estimation. *J. Geophys. Res.*, **94**, 14215- 14225
815

816 Chernet, T, 2012, Dallol Volcano and Danakil Depression, Ethiopia, Magmatic
817 Rifting and Active Volcanism conference, Addis Ababa,
818 <http://www.see.leeds.ac.uk/afar/new-afar/conference/talks/Tadiwos.pdf>
819

820 Counil, J-L, Le Mouél, J-L & Menvielle, M., 1986. Associate and conjugate direction
821 concepts in magnetotellurics, *Ann. Geophys.*, **4**, 115-130
822

823 Daniels, K A, Bastow, I D, Keir, D, Sparks, R S J and Menand, T, 2014. Thermal
824 models of dyke intrusion during development of continent–ocean transition, *Earth*
825 *Planet. Sci. Lett.*, **385**, 145-153, doi: 10.1016/j.epsl.2013.09.018
826

827 Desissa, M, *et al.*, 2013, A mantle magma reservoir beneath an incipient mid-ocean
828 ridge in Afar Ethiopia, *Nature Geosci.*, **6**, 861-865, doi: 10.1038/ngeo1925
829

830 Didana, Y L, Thiel, S and Heinson, G, 2014, Magnetotelluric imaging of upper crustal
831 partial melt at Tendaho graben in Afar, Ethiopia, *Geophys. Res. Lett.*, **41**, 3089-3095,
832 doi: 10.1002/2014GL060000
833

834 Ebinger, C J, *et al.*, 2008, Capturing magma intrusion and faulting processes during
835 continental rupture: seismicity of the Dabbahu (Afar) rift, *Geophys. J. Int.*, **174**, 1138–
836 1152
837

838 Ebinger, C, *et al.*, 2010, Length and Timescales of Rift Faulting and Magma
839 Intrusion: The Afar Rifting Cycle from 2005 to Present, *Ann. Rev. Earth Planet. Sci.*,
840 **38**, 437–64
841

842 Ferguson, D, *et al.*, 2010, Recent rift-related volcanism in Afar, Ethiopia, *Earth*
843 *Planet. Sci. Lett.*, **292**, 409-418
844

845 Ferguson, D J, *et al.*, 2013, Melting during late-stage rifting in Afar is hot and deep,
846 *Nature*, **499**, 70-73
847
848 Ferguson, I J, 2012. Instrumentation and Field Procedure, Chapter 9 in *The*
849 *Magnetotelluric Method: Theory and Practice*, ed. Chave, A D and Jones, A G, p421-
850 479, Cambridge University Press, Cambridge, UK
851
852 Field, L P, Blundy, J, Brooker, R A, Wright, T J and Yirgu, G, 2012, Magma storage
853 conditions beneath Dabbahu Volcano (Ethiopia) constrained by petrology, seismicity
854 and satellite geodesy, *Bull. Volcanol.*, **74**, 981–1004
855
856 Field, L P, Blundy, J, Calvert A and Yirgu, G, 2013, Magmatic history of Dabbahu, a
857 composite volcano in the Afar Rift, Ethiopia, *GSA Bull.*, **125**, 128-147, doi:
858 10.1130/B30560.1
859
860 Grandin, R, *et al.*, 2010, Transient rift opening in response to multiple dike injections
861 in the Manda Hararo rift (Afar, Ethiopia) imaged by time-dependent elastic inversion
862 of interferometric synthetic aperture radar data, *J. Geophys. Res.*, **115**, B09403,
863 doi:10.1029/2009JB006883

864 Groom, R W & Bailey, R C, 1989. Decomposition of magnetotelluric impedance
865 tensors in the presence of local 3-dimensional galvanic distortion, *J. Geophys. Res.*,
866 **94**, 1913-1925

867 Guidarelli, M., *et al.*, 2011. Surface wave tomography across Afar, Ethiopia: Crustal
868 structure at a rift triple-junction zone, *Geophys. Res. Lett.*, **38**, L24313,
869 doi:10.1029/2011GL046840
870
871 Hamling, I J, Ayele, A, Bennati, L, Calais, E and Ebinger, C J, 2009, Geodetic
872 observations of the ongoing Dabbahu rifting episode: new dyke intrusions in 2006 and
873 2007, *Geophys. J. Int.*, **178**, 989-1003
874
875 Hammond, J O S, *et al.*, 2011, The nature of the crust beneath the Afar triple junction:
876 Evidence from receiver functions, *Geochem. Geophys. Geosys.*, **12**, Q12004, doi:
877 1029/2011GC003738
878
879 Hashin, Z and Shtrikman, S, 1962, A variational approach to the theory of the
880 effective magnetic permeability of multiphase materials. *J. Appl. Phys.*, **33**, 3125-
881 3131
882
883 Häuserer M and Junge A, 2011, Electrical mantle anisotropy and crustal conductor: a
884 3-D conductivity model of the Rwenzori Region in western Uganda, *Geophys. J. Int.*,
885 **185**, 1235–1242
886
887 Hautot, S, *et al.*, 2000, The deep structure of the Baringo rift Basin (central Kenya)
888 from 3-D magnetotelluric imaging: Implications for rift evolution, *J. Geophys. Res.*,
889 **105**, 23,493-23,518
890
891 Hautot, S, *et al.*, 2012, Melt distribution between the crust and mantle beneath the
892 Dabbahu-Manda Hararo rift segment, Afar, from 3D magnetotelluric imaging,

- 893 Magmatic Rifting and Active Volcanism conference, Addis Ababa,
894 <http://www.see.leeds.ac.uk/afar/new-afar/conference/talks/Hautot.pdf>
895
- 896 Hayward, N and Ebinger, C, 1996, Variations in along-axis segmentation of the Afar
897 Rift System, *Tectonics*, **15**, 244-257
898
- 899 Heinson, G, Constable, S and White, A, 2000, Episodic melt transport at mid-ocean
900 ridges inferred from magnetotelluric sounding. *Geophys. Res. Lett.*, **27**, 2317-2320
- 901 Hovland, M, Rueslaatten, H and Johnsen, H K, 2008, Hydrothermal salt—but how
902 much?: Reply to Christopher Talbot on his comments to our articles, *Marine Petrol.*
903 *Geol.*, **25**, 203-4
- 904 Jones, A G and Ferguson, I J, 2001. The electric Moho. *Nature*, **409**, 331-333
905
- 906 Kalberkamp, U, 2009, Magnetotelluric measurements to explore for deeper structures
907 of the Tendaho geothermal field, Afar, NE Ethiopia, 23rd Kolloquium
908 Elektromagnetische Tiefenforschung, Seddiner See, Germany
909
- 910 Karson, J P, *et al.*, 1987. Along-axis variations in seafloor spreading in the MARK
911 area, *Nature*, **328**, 681-685
912
- 913 Keir, D, *et al.*, 2009, Evidence for focused magmatic accretion at segment centers
914 from lateral dike injections captured beneath the Red Sea rift in Afar, *Geology*, **37**,
915 59–62
- 916 Keir, D, Belachew, M, Ebinger, C J, Kendall, J-M, Hammond, J O S, Stuart, G W,
917 Ayele A and Rowland J V, 2011, Mapping the evolving strain field during continental
918 breakup from crustal anisotropy in the Afar depression, *Nat. Commun.*, **2:285**, doi:
919 10.1038/ncomms1287
- 920 Kelbert, A, Egbert, G D and DeGroot-Hedlin, C, 2012, Crust and upper mantle
921 electrical conductivity beneath the Yellowstone Hotspot Track, *Geology*, **40**, 447-
922 450, doi: 10.1130/G32655.1
- 923 Key, K, Constable, S, Liu, L and Pommier, A, 2013. Electrical image of passive
924 upwelling beneath the northern East Pacific Rise, *Nature*, **495**, 499-502
- 925 Lahitte, P, Gillot, P Y and Courtillot, V, 2003, Silicic central volcanoes as precursors
926 to rift propagation: the Afar case. *Earth Planet. Sci. Lett.*, **207**, 103–116
- 927 Lemma, Y and Hailu, A, 2006, Gravity and magnetics survey at the Tendaho
928 geothermal field, Geological Survey of Ethiopia, Addis Ababa, Ethiopia, 23pp
929 (unpublished)
930
- 931 MacLennan, J, McKenzie, D, Gronvöld, K and Slater, L, 2001, Crustal accretion under
932 northern Iceland, *Earth Planet. Sci. Lett.*, **191**, 295-310
933
- 934 MacGregor, L M, Constable, S and Sinha, M C, 1998, The RAMESSES experiment –
935 III. Controlled-source electromagnetic sounding of the Reykjanes Ridge at 57°45'N.
936 *Geophys. J. Int.*, **135**, 773-789

937
938 Magde, L S, Sparks, D W and Detrick, R S, 1997, The relationship between buoyant
939 mantle flow, melt migration, and gravity bull's eyes at the Mid-Atlantic Ridge
940 between 33°N and 35°N, *Earth Planet. Sci. Lett.*, **148**, 59-67
941
942 McNeice, G W and Jones, A G, 2001, Multisite, multifrequency tensor decomposition
943 of magnetotelluric data, *Geophysics*, **66**, 158-173
944
945 Medynski, S, *et al.*, 2015, Stability of rift axis magma reservoirs: spatial and temporal
946 evolution of magma supply in the Dabbahu rift segment (Afar, Ethiopia) over the past
947 30 kyr, *Earth Planet. Sci. Lett.*, **409**, 278-289, doi: 10.1016/j.epsl.2014.11.002
948
949 Miensopust, M P, Jones, A G, Hersir, G P and Vilhjalmsón, A M, 2014, The
950 Eyjafjallajökull volcanic system, Iceland: insights from electromagnetic
951 measurements, *Geophys. J. Int.*, **199**, 1187-1204, doi: 10.1093/gji/ggu322
952
953 Munoz, G, 2014, Exploring for Geothermal Resources with Electromagnetic Methods,
954 *Surv. Geophys.*, **35**, 101-122, doi: 10.1007/s10712-013-9236-0
955
956 Parker, R L and Booker, J R, 1996, Optimal one-dimensional inversion and bounding
957 of magnetotelluric apparent resistivity and phase measurements, *Phys. Earth Planet.*
958 *Ints.*, **98**, 269-282
959
960 Pommier, A and Le Trong, E, 2011, SIGMELTS: A web portal for electrical
961 conductivity calculations in geosciences, *Comp. Geosci.*, **37**, 1450-1459
962
963 Ritter O, Junge A and Dawes G J K, 1998, New equipment and processing for
964 magnetotelluric remote reference observation. *Geophys. J. Int.*, **132**, 535-548
965
966 Roberts, J J and Tyburczy, J A 1999, Partial-melt electrical conductivity: Influence of
967 melt composition, *J. Geophys. Res.*, **104**, 7055-7065
968
969 Rowland, J V, *et al.*, 2007, Fault growth at a nascent slow-spreading ridge: 2005
970 Dabbahu rifting episode, Afar, *Geophys. J. Int.*, **171**, 1226–1246
971
972 Schmeling, H, 1985, Numerical models on the influence of partial melt on elastic,
973 anelastic and electric properties of rocks. Part I: Elasticity and anelasticity, *Phys.*
974 *Earth Planet. Inter.*, **41**, 34–57
975
976 Simpson F, 2000, A three-dimensional model of the southern Kenya rift: departure
977 from two dimensionality as a possible consequence of a rotating stress field, *J.*
978 *Geophys. Res.*, **105**, 19321–19334
979
980 Simpson, F and Bahr, K, 2005, *Practical Magnetotellurics*. Cambridge University
981 Press, Cambridge, UK
982
983 Singh, S C, *et al.*, 2006. Discovery of a magma chamber and faults beneath a Mid-
984 Atlantic Ridge hydrothermal field, *Nature*, **442**, 1029-1032

985 Sinha, M C, *et al.*, 1997. Evidence for accumulated melt beneath the slow-spreading
986 Mid-Atlantic Ridge, *Phil. Trans. R. Soc. Lond. A*, **355**, 233-253
987
988 Siripunvaraporn, W and Egbert, G, 2000, An efficient data sub-space inversion
989 method for 2-D magnetotelluric data, *Geophysics*, **65**, 791-803
990
991 Sternberg, B, Washburne, J C and Pellerin, L, 1988, Correction for the static shift in
992 magnetotellurics using transient electromagnetic soundings, *Geophysics*, **53**, 1459-
993 1468
994
995 Stork, A L, Stuart, G W, Henderson, C M, Keir, D and Hammond, J O S, 2013,
996 Uppermost mantle (P_n) velocity model for the Afar region, Ethiopia: An insight into
997 rifting processes, *Geophys. J. Int.*, **193**, 321-328 (2013)
998
999 Talbot, C, 2008, Hydrothermal salt – but how much? *Marine Petrol. Geol.*, **25**, 191-
1000 202
1001
1002 Toomey, D R, *et al.*, 2007. Skew of mantle upwelling beneath the East Pacific Rise
1003 governs segmentation, *Nature*, **446**, 409-414
1004
1005 Wannamaker, P E *et al.*, 2008, Lithospheric dismemberment and magmatic processes
1006 of the Great Basin-Colorado Plateau transition, Utah, implied from magnetotellurics,
1007 *Geochem. Geophys. Geosyst.*, **9**, Q05019, doi: 10.1029/2007GC001886
1008
1009 Weaver, J, 1994, *Mathematical methods for geo-electromagnetic induction*. Research
1010 Studies Press
1011
1012 Wright, T J, *et al.*, 2006, Magma-maintained rift segmentation at continental rupture
1013 in the 2005 Afar dyking episode, *Nature*, **442**, 291–294
1014

1015 Figure Captions

1016

1017 Figure 1. Tectono-magmatic segmentation of the Afar volcanic province, after
1018 Hayward and Ebinger (1996). TGD denotes the Tendaho-Goba'ad discontinuity.
1019 Earthquake fault plane solutions indicate predominantly normal faulting. Small black
1020 dots indicate epicentres of earthquakes recorded October 2005 – April 2006 by a
1021 regional temporary seismic array, as described by Ebinger et al. (2008). The box
1022 shows the area of Figure 2.

1023

1024 Figure 2. Magnetotelluric site distribution along three profiles, superimposed on the
1025 topography: to the north, across (Dabbahu line) and oblique (Teru line) to the active
1026 Dabbahu magmatic segment; to the south, across (Hararo line) the inactive Hararo
1027 segment. In red, the star marks the site of the 2009 eruption within the Ado'Ale
1028 Volcanic Complex (AVC) and the Badi and Dabbahu volcanoes are labelled. The red
1029 lines delineate the region of the Dabbahu magmatic segment intruded in the recent
1030 dyking episode. The dashed black line indicates the locus of the rift axis through the
1031 Hararo magmatic segment.

1032

1033 Figure 3. Scaled TEM decay curves (green symbols) overlain on TE and TM mode
1034 apparent resistivity curves (blue and red symbols respectively). Site numbers given in
1035 the top left of the plot.

1036

1037 Figure 4. Data pseudo-section for the Hararo profile, with sites arranged from west to
1038 east. Upper panels are apparent resistivity, lower panels phase. Left-hand side is TE
1039 mode, right-hand side the TM mode. Grey masks areas of missing data.

1040

1041 Figure 5. As for Figure 4 for the Teru profile, with sites plotted south to north.

1042

1043 Figure 6. Resistivity structure beneath the three profiles, embedded in a 3D volume of
1044 the region. The Hararo profile is on the right, the Teru profile on the left, and the
1045 Dabbahu profile between them. The red crosses are the sites, the red lines show the
1046 location of dykes intruded in the current episode, B, D and G are the Badi, Dabbahu
1047 and Gab'ho volcanoes respectively, AVC is the Ado'Ale Volcanic Complex, and the
1048 black dotted line on the Hararo profile marks the rift axis of that segment. The
1049 resistivity scale beneath applies to all three models, with substantial parts of the Teru
1050 model saturated at the low resistivity limit.

1051

1052 Figure 7. Data fits for the Hararo profile model, that furthest to the right in Figure 6,
1053 from west to east along the profile. Blue (red) symbols and curves are the TE (TM)
1054 data and model predictions, respectively. Error bars are one standard deviation. Site
1055 numbers are indicated in the top left corner.

1056

1057 Figure 8. Data fits for the Teru profile model, furthest to the left in Figure 6, from
1058 south to north along the profile. Legend as for Figure 7.

1059

1060 Figure 9. Sill-like model of the deeper conductor beneath the Dabbahu profile.

1061

1062 Figure 10. Fits to the Dabbahu profile data. Bold colour curves are the predictions of
1063 the sill-like model of Figure 9; lighter colour curves are those of the original model

1064 shown in Figure 6. At most sites and periods, the differences are indistinguishable by
1065 eye. Legend as for Figure 7.

1066

1067 Figure 11. Blocks of the Teru profile minimum structure resistivity model colour-
1068 coded according to their melt amount, for an assumed melt resistivity of $0.1 \Omega\text{m}$ and
1069 the parallel conducting pathways model. Yellow corresponds to pure melt. The
1070 vertical line indicates the assumed axis of symmetry of the conductor when inferring
1071 melt volume (see text for details).

1072

1073 Figure 12. Summary cartoon of melt distribution beneath the Dabbahu and Hararo
1074 (sometimes referred to collectively as Manda-Hararo) magmatic segments looking
1075 approximately north-east, inferred from magnetotelluric data, with support from
1076 petrological, seismic, remote sensing and geological information. Blue dashed lines
1077 show the locations of the three magnetotelluric profiles.

1078

1079 Table caption

1080

1081 Table 1. Root-mean-square misfits for each site and overall of the ‘strike’
1082 decomposition model applied simultaneously to the Hararo (top) and Teru (bottom)
1083 profiles for their preferred geoelectrical strike directions. Sites are listed from west to
1084 east for the Hararo profile, and south to north for the Teru profile.

1085

1086

1087

1088

1089

1090

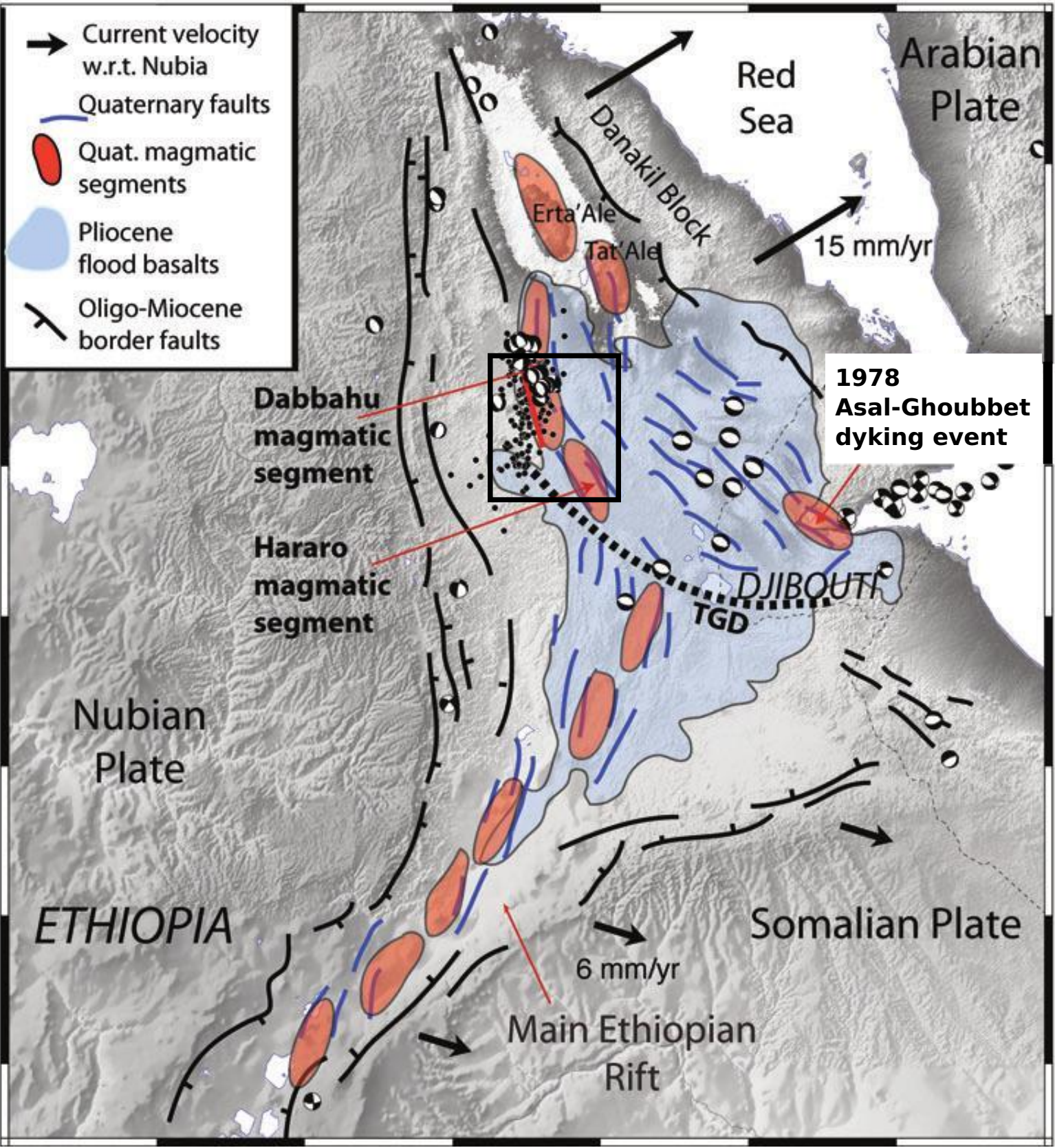
1091

38

40

42

44



40°30'

41°00'

12°30'

12°30'

12°00'

12°00'

40°30'

41°00'

TERU LINE

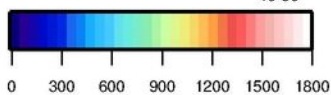
Dabbahu

Badi

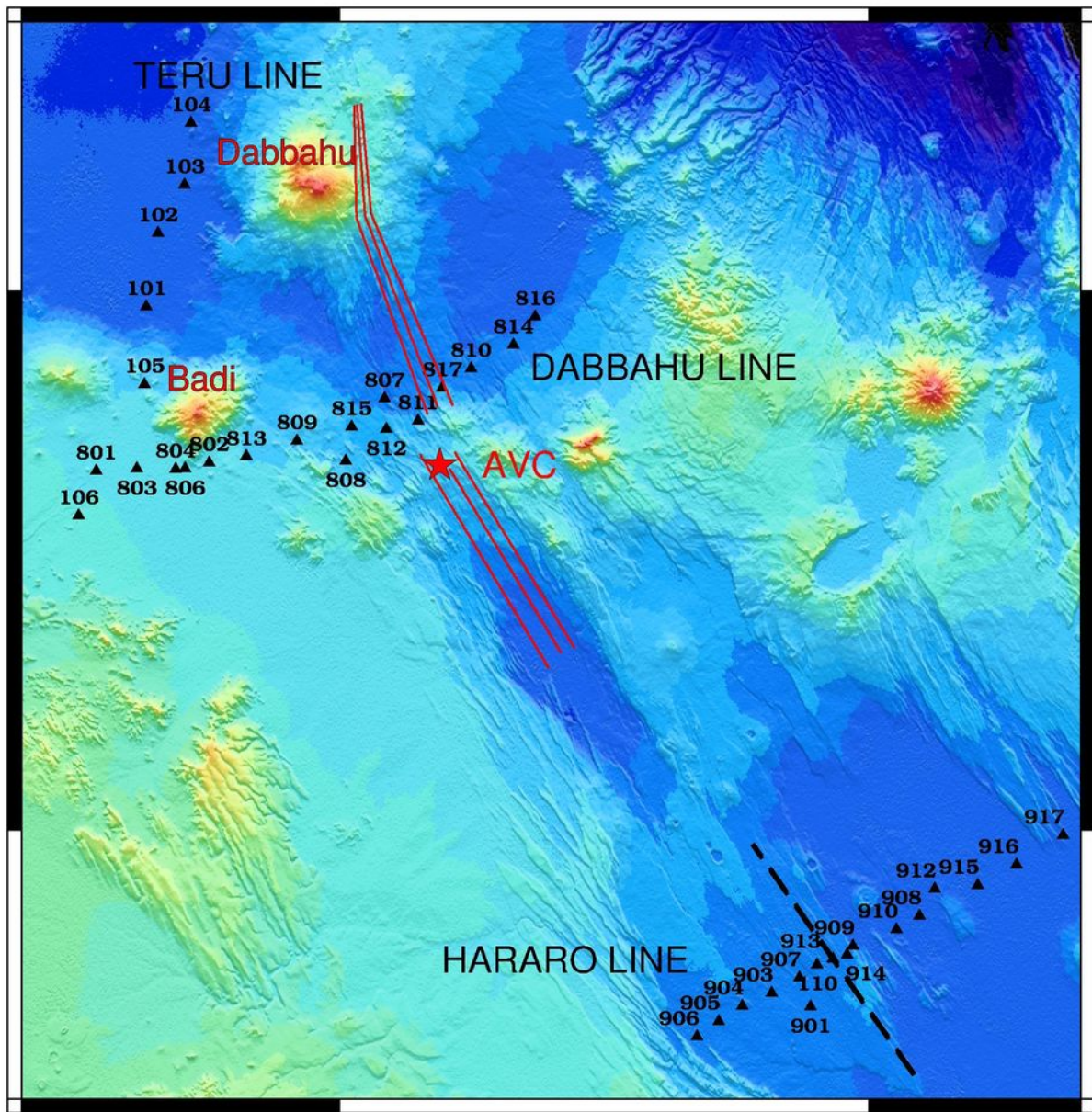
DABBAHU LINE

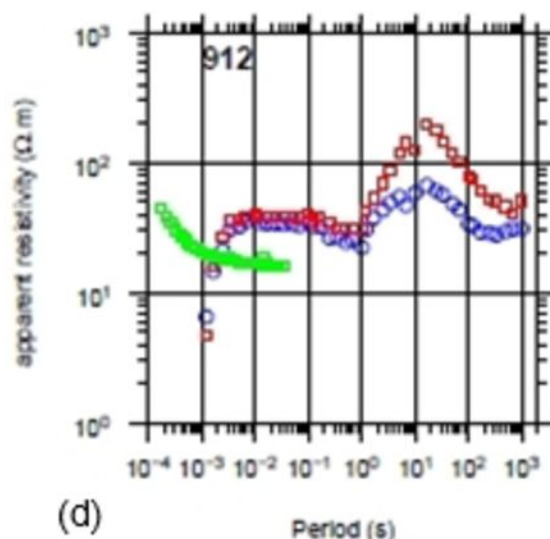
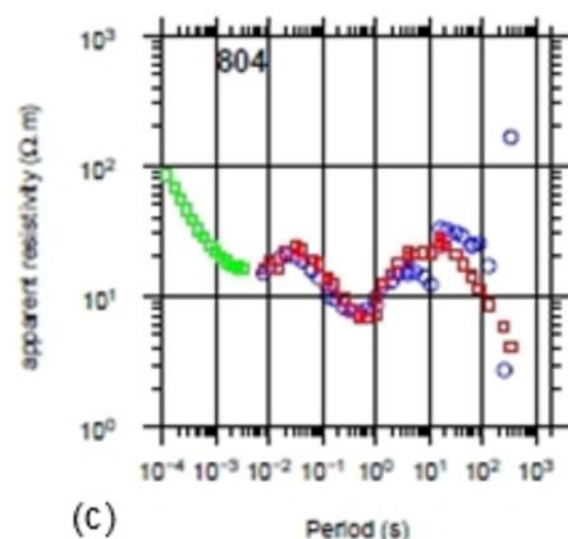
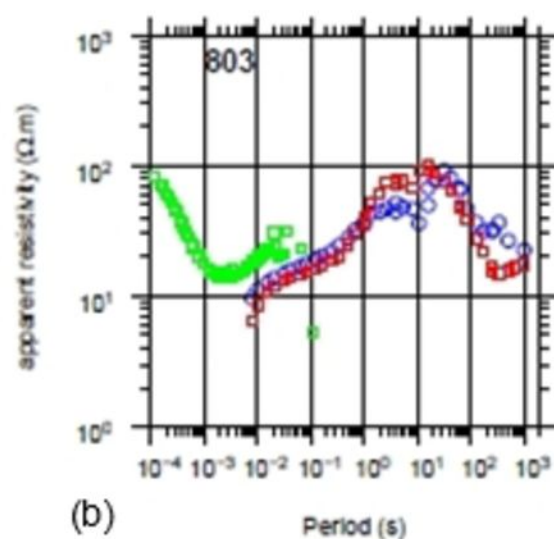
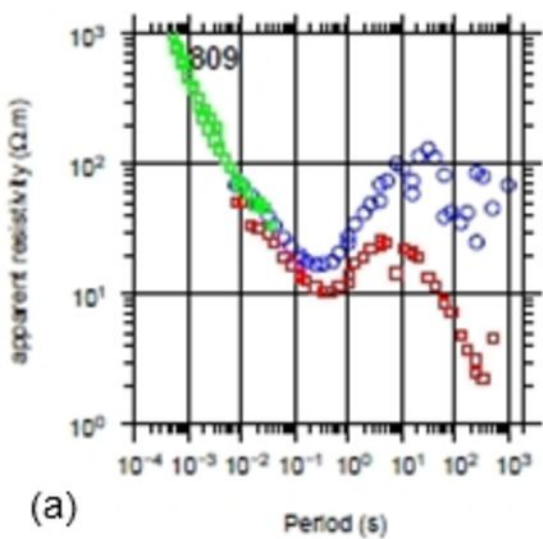
AVC

HARARO LINE

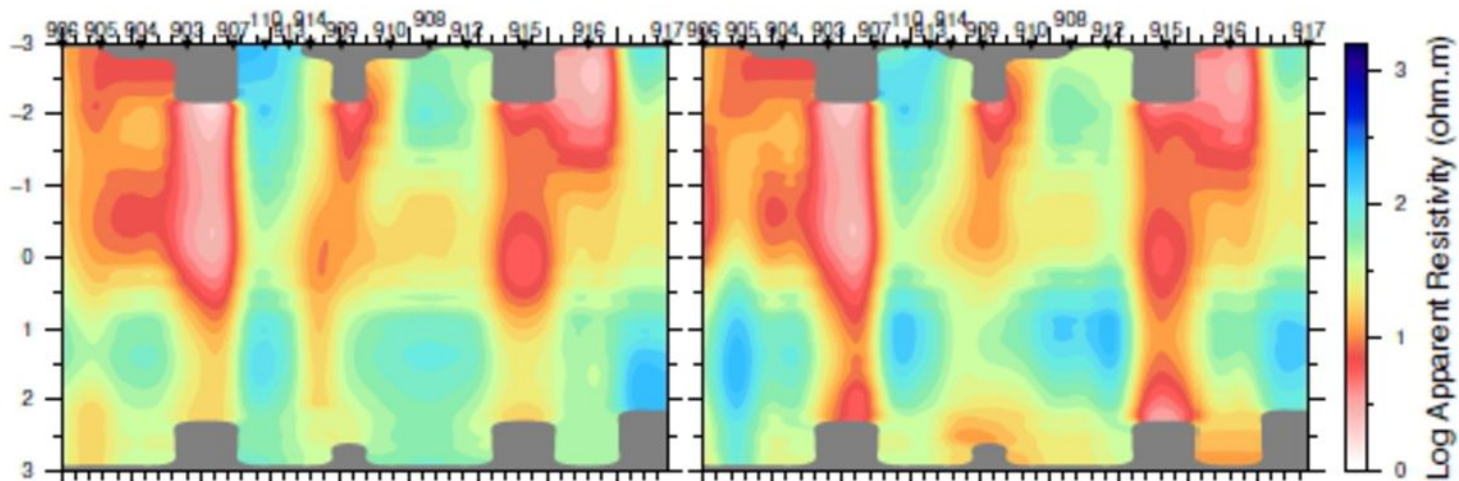


metres

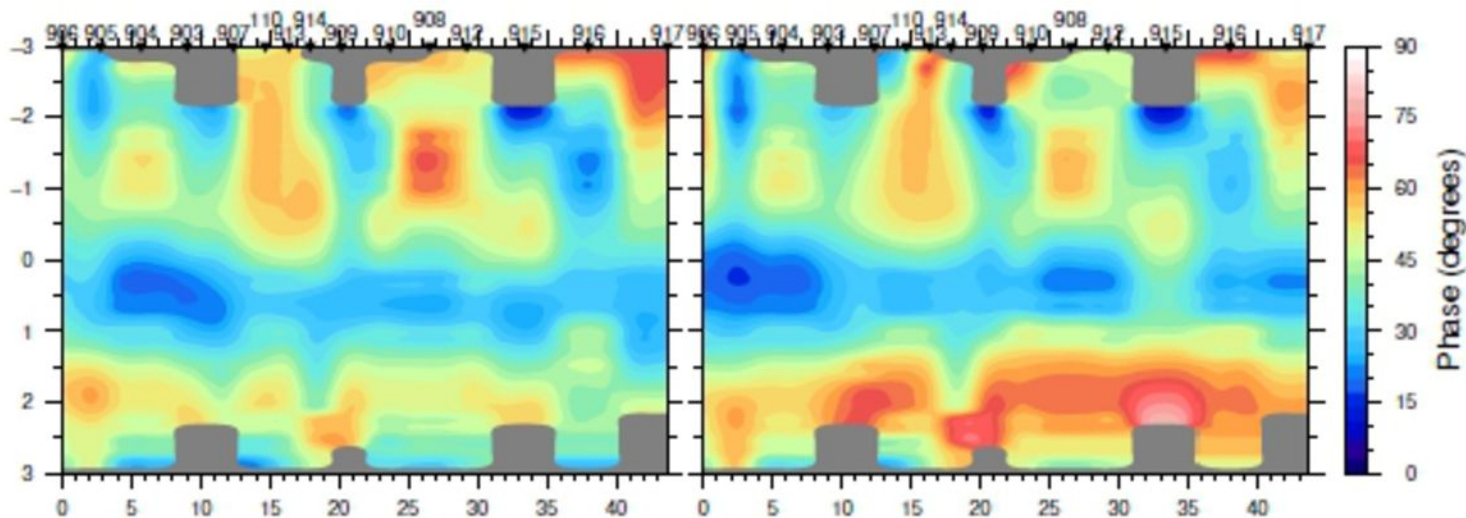


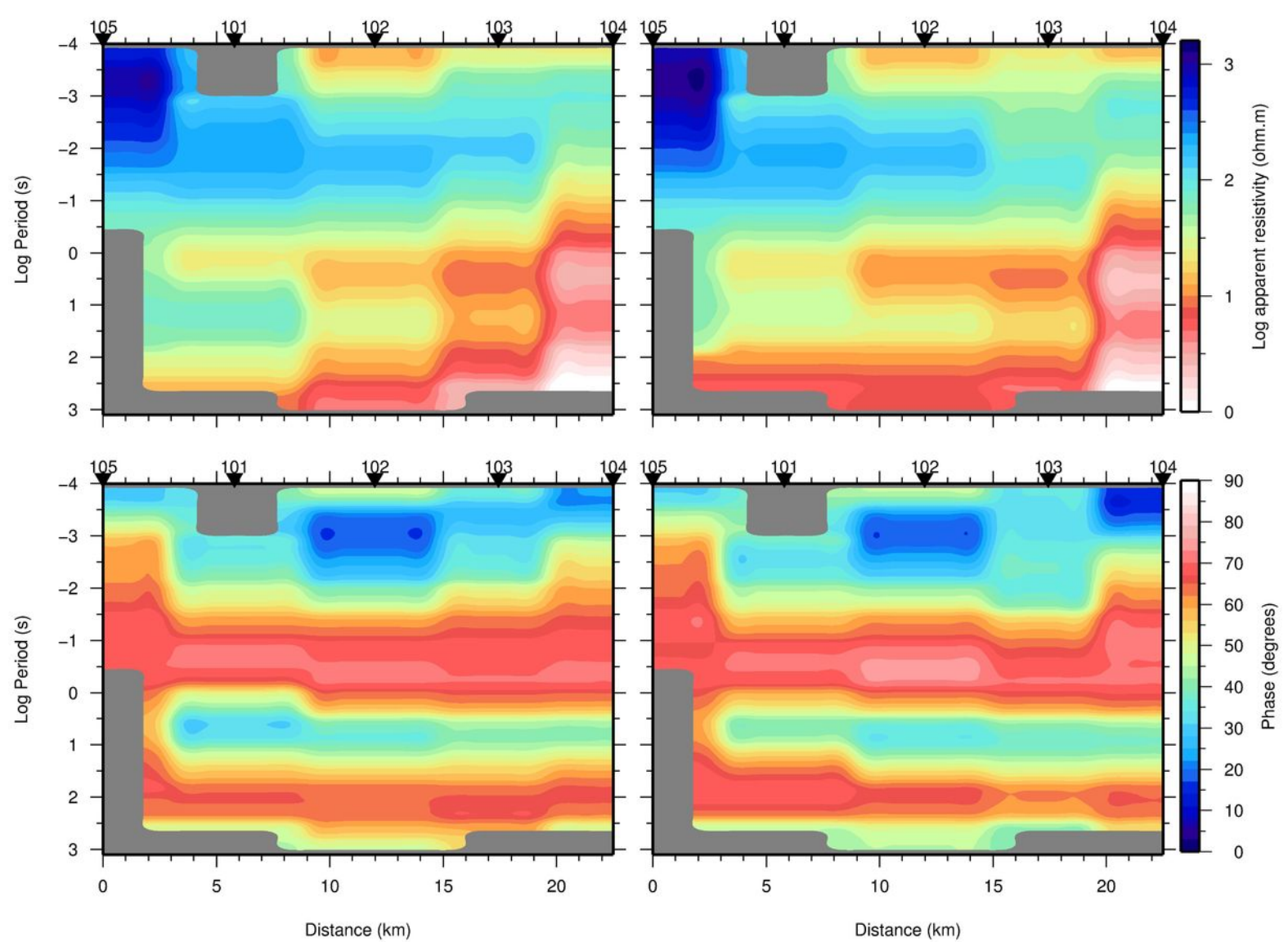


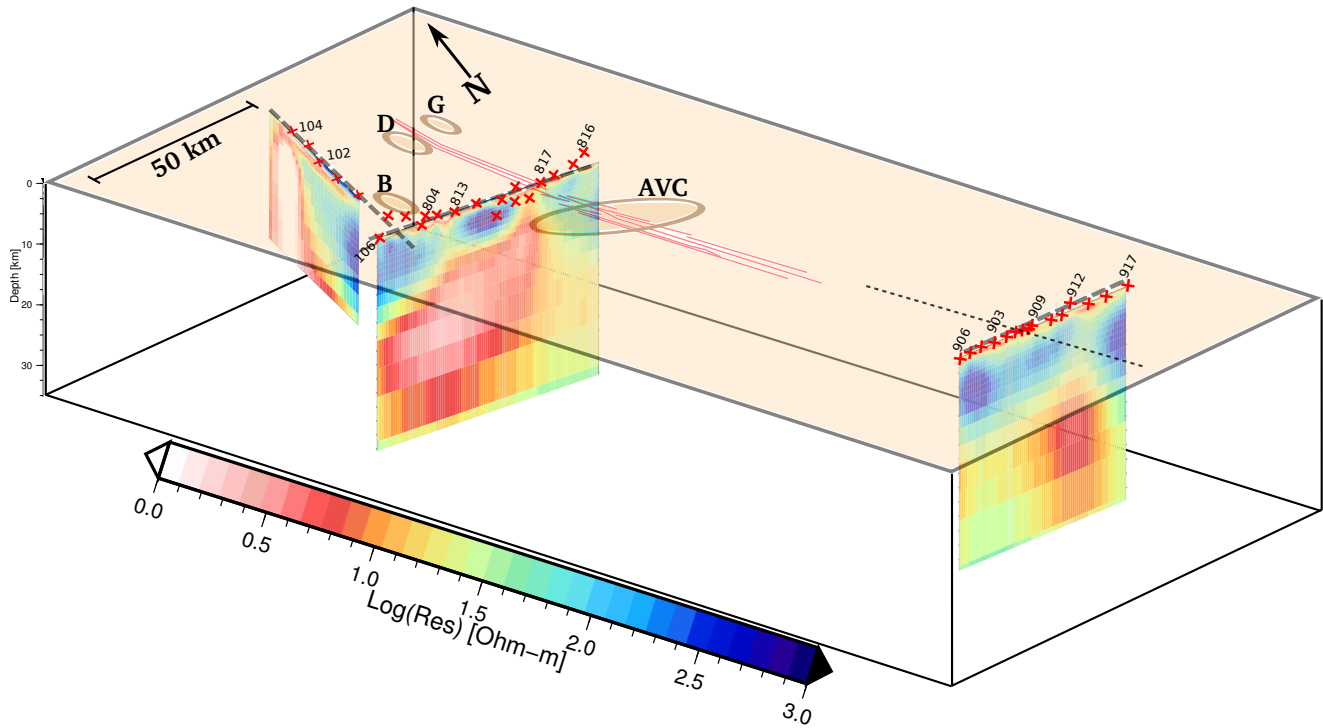
Log Period (s)

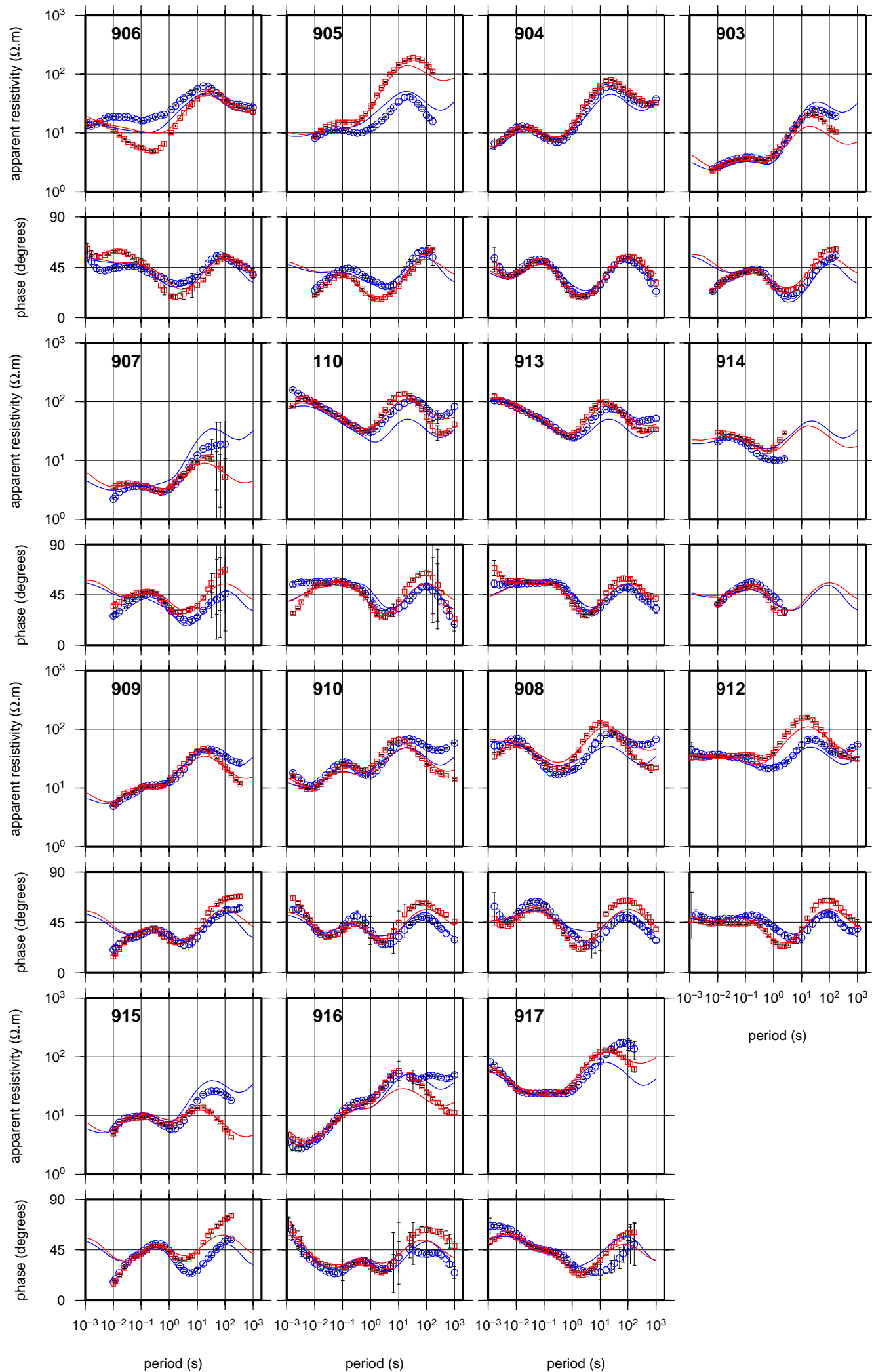


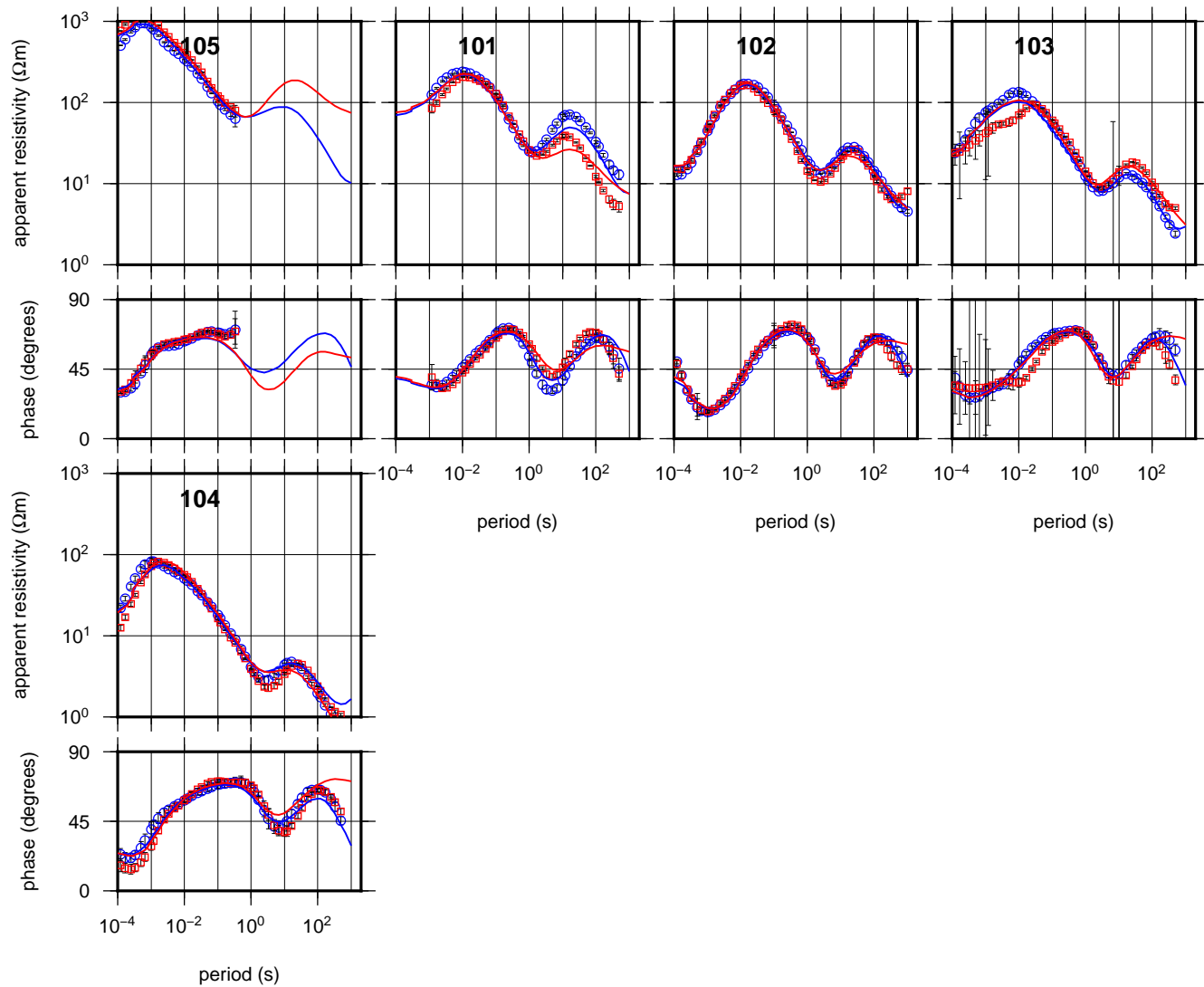
Log Period (s)

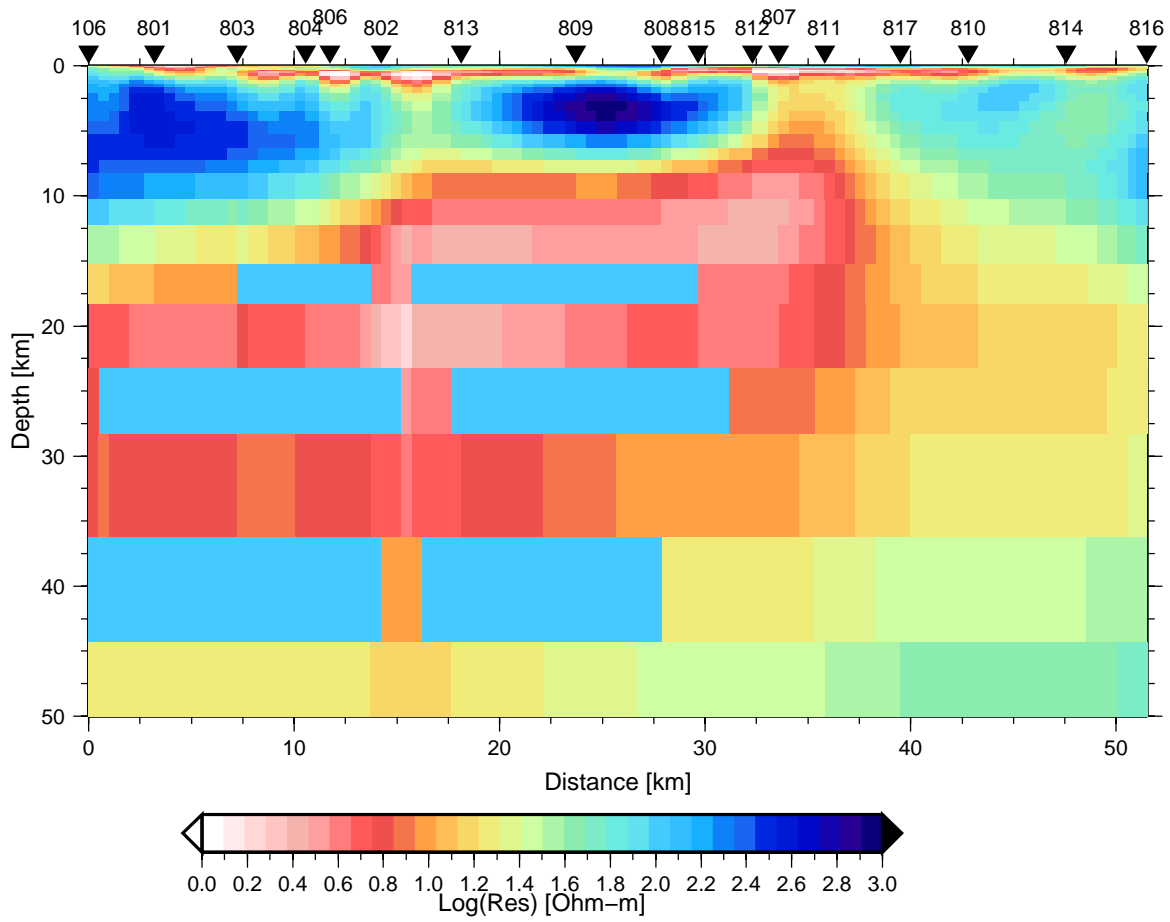


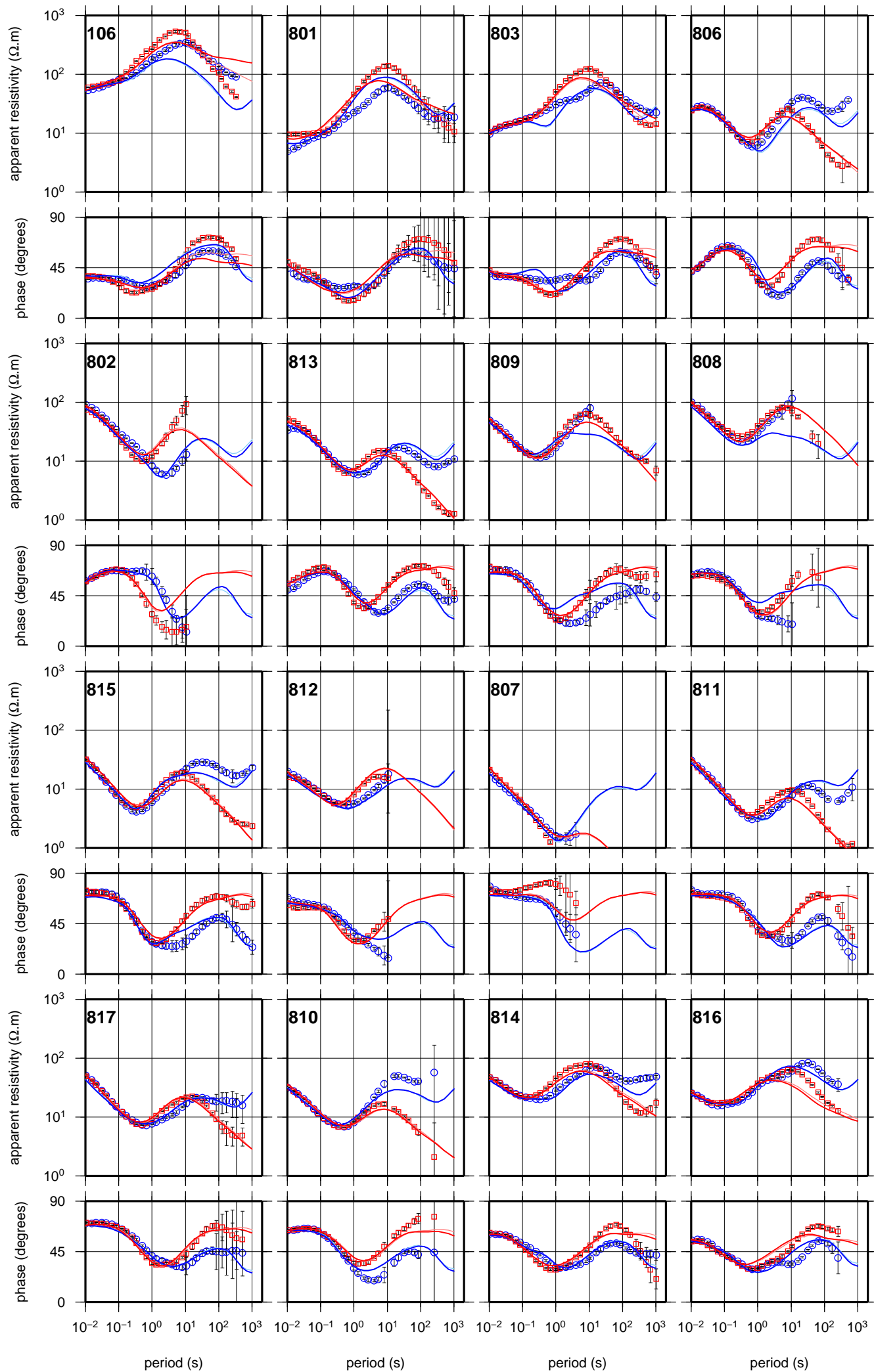


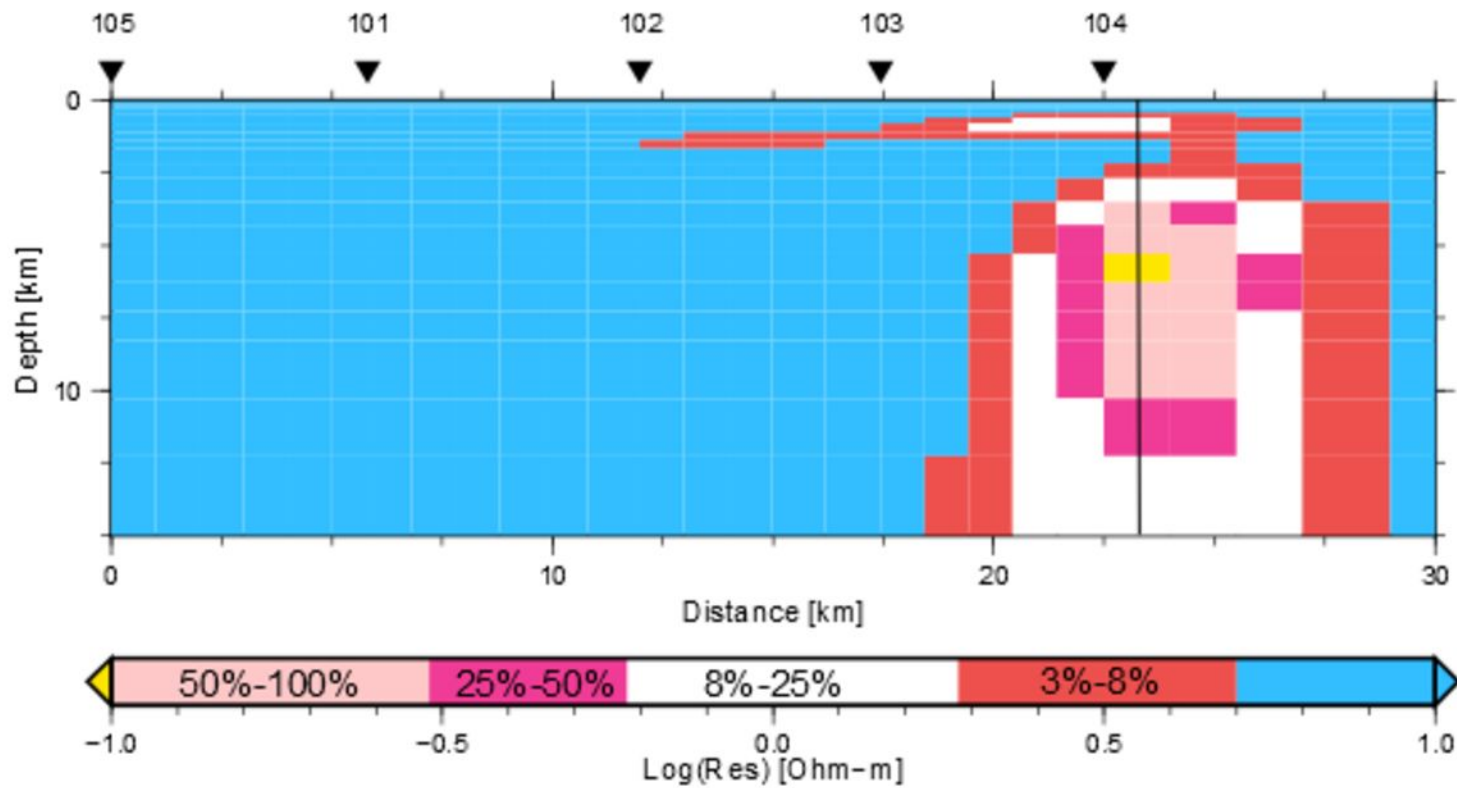


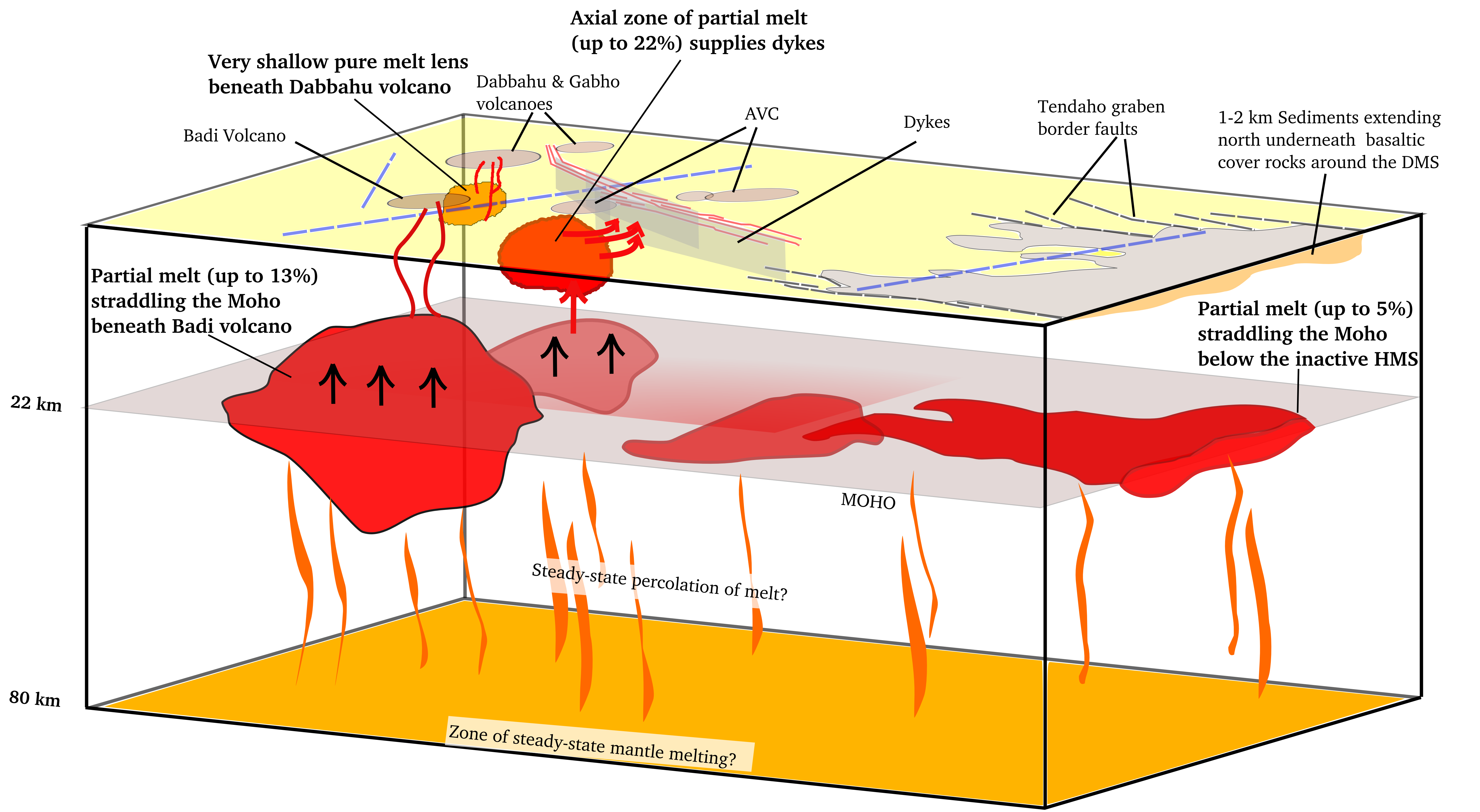












| | | | | | | | | | |
|----------|-----|-----|-----|-----|---------|-----|---------|-----|-----|
| Site 906 | 905 | 904 | 903 | 907 | 110 | 913 | 914 | 909 | |
| Misfit | 0.8 | 0.6 | 1.1 | 1.3 | 1.4 | 1.2 | 1.2 | 1.4 | 1.8 |
| Site 910 | 911 | 908 | 912 | 915 | 916 | 917 | Overall | | |
| Misfit | 0.7 | 1.2 | 1.4 | 1.4 | 0.8 | 1 | 1.5 | 1.2 | |
| Site 105 | 104 | 103 | 102 | 101 | Overall | | | | |
| Misfit | 1.4 | 1.9 | 1.7 | 1.4 | 1.3 | 1.6 | | | |